UiO : University of Oslo

Structural Characterization of High Entropy Metal Silicide Alloys

An investigation of the Si:Cr:Fe:Co:Ni:Cu system

Mari Mathillas Røsvik

A thesis presented for the degree of
Master of Science

Materials Science for Energy and Nanotechnology
60 credits

Department of Physics
University of Oslo
Norway

Figure 1: link to source: https://xkcd.com/683/

Acronyms

ABF annular bright field

ADF annular dark field

BF bright field

BSE back-scattered electrons

DF dark field

DFT density functional theory

DP diffraction pattern

EDS X-ray energy dispersive spectroscopy

FEG field-emission gun

FFT fast Fourier transform

FOLZ first-order Laue zone

HAADF high-angle annular dark field

HEA high entropy alloy

HMS higher manganese silicide

HOLZ higher-order Laue zone

MPEA multi-principal element alloy

SAED selected area electron diffraction

SE secondary electron

SEM scanning electron microscope

SS solid solution

STEM scanning transmission electron microscope

TE thermoelectric

TEG thermoelectric generator

TEM transmission electron microscope

VLM visible light microscope

XRD X-ray diffraction

ZA zone axis

ZOLZ zero-order Laue zone

Acknowledgements

There are many people without whom this thesis would never have seen the light of day. First and foremost, I have to say a very big thank you to my wonderful supervisors, Anette Gunnæs, Patricia Carvalho, and Matthias Schrade. Your knowledge and interest has been worth so much, and you have always made me feel that it was okay to reach out with stupid questions (of which there have been many). Many of the experiments necessary for this project would also not have been possible because of Covid restrictions, without your effort, and for that, I am extremely grateful.

I also wish I could thank every member of the Structure Physics research group by name for creating an open environment where it's always okay to ask for help, and discussions around tricky scientific subjects are always welcome. I would especially like to thank Ole Bjørn Karlsen, for valuable help with interpretation and implementation of XRD experiments, and Phuong Nguyen for SO much help and guidance when I am clueless about TEM operation.

To all of my wonderful friends helping with proofreading, advice and emotional support; thank you so, so much. Writing a master thesis can be extremely challenging at times, and it is so incredibly valuable to know you are not alone.

Last, but by no means least, to my wonderful boyfriend, Mikael Kiste; you have been there through all of my ups and downs on this project, have listened to my incomprehensible rants on difficult problems for countless hours and have never stopped cheering me on. You have offered so much support, both moral, emotional and technical (yes, I know I'm a bit technically challenged, thank you for being patient with me). Vi er dinosaurer, *hodedunk*.

Contents

Chapter 1

Introduction

1.1 Motivation

Low carbon energy production has been the subject of countless conversations, news articles, and research papers. Many different kinds of renewable and low-carbon energy technologies, such as solar and wind farms, are in development and being implemented around the world. In the quest for a sustainable energy future, there will be a need for many different kinds of low-carbon energy technologies to accommodate different situations and requirements. Not all places have reliable access to wind and sun, for instance. Thermoelectric generators (TEGs) can have the potential to be an alternative (or an addition) for sustainable electrical energy production by converting waste heat into usable electrical energy, without any moving parts. Thermoelectric technology combines additional advantages, like longevity and noiselessness operation. Thermoelectric materials find further application areas in active cooling through the reverse thermoelectric effect, or as temperature and heat flux sensors [1]. There are, however, some challenges that will have to be solved before some of these technologies can become viable on a commercial scale.

Briefly stated, TEGs work by converting a heat gradient into an electric current. The efficiency with which this happens is determined by the properties of the thermoelectric materials in the generator and can be expressed as a function of the dimensionless thermoelectric figure of merit, zT.

$$zT = \frac{\sigma S^2}{\kappa_{el} + \kappa_{ph}}T \qquad (1.1)$$

Good thermoelectric (TE) materials should be semiconductors with high electrical conductivity, σ, and Seebeck coefficient, S and a low thermal conductivity. The thermal conductivity can be divided into an electronic contribution, κ_{el} of the charge carriers and a contribution of lattice vibrations, κ_{ph}. Unfortunately, the σ and κ_{el} are closely related via the Wiedemann-Franz law [2, p.156]. The best thermoelectric converters can reach efficiencies around 10-20% of the Carnot efficiency, corresponding to a figure of merit of around $0.5 \leq ZT \leq 1.5$ [3].
The parameters deciding the value of zT are highly correlated, and changing one often leads to changes in the others. Thus, finding a good thermoelectric material is a complex and difficult task.
So far, many of the most efficient thermoelectric materials that have been developed are toxic or based on elements with a low abundance in Earth's crust, such as lead (Pb), tellurium (Te), antimony (Sb), germanium (Ge), ytterbium (Yb), bismuth (Bi), selenium (Se) and silver (Ag). (Ga)[4][5][6][7]. Toxicity and low abundance are two factors quite clearly counting against scalability for these materials, and for that reason, other materials are needed.

Silicides are an attractive materials class for energy uses because they are often non-toxic, stable over wide temperature ranges, and cheap as they are made up of abundant elements. Many silicides are also proven to have promising thermoelectric properties [8], and much research has gone into improving their properties, for example by increasing the power factor, σS^2 by doping or lowering thermal conductivity through nanostructuring. However, despite extensive research efforts, only a few silicides have been found to exhibit zT larger than 1 [8].

High entropy alloys (HEAs) are a relatively new group of materials that have displayed many interesting structural and functional properties. Among these is a reported low thermal conductivity at lower temperatures, when compared to pure metals, as well as a much weaker temperature dependency for these properties [9]. Most of the research into HEAs thus far has focused on the mechanical properties and not the functional, consequently there is a lot of new ground to be broken when it comes to research into this materials class.

This thesis is a part of a larger research project, ANSWER, which is a collaboration between UiO, SINTEF and the German Aerospace Center (DLR). My supervisors have been Anette Gunnæs (UiO), Patricia Carvalho (SINTEF) and Matthias Schrade (SINTEF). This project addresses the question, whether applying the high-entropy alloy concept to silicides can produce thermoelec-

tric materials with high figures of merit. This thesis has focused specifically on the M_2Si-system (M=Co,Cr,Cu,Fe,Ni) and on identifying and investigating metal silicides with high entropy on the metal site. The main focus of this master project has been on structural and microstructural characterization of the system, but some effort has also gone into screening of the identified materials for their thermoelectric properties.

1.2 Literature Review

In this section, an attempt will be made to give an overview of the current state of research into the fields most relevant to this project. As there exists little to no data into the thermoelectric properties of silicon based HEAs, this section has instead been written about thermoelectric silicides and the properties of high entropy alloys separately.

1.2.1 Thermoelectric Silicides

Silicides have been investigated for thermoelectric purposes since 1958, so the field of thermoelectric silicides is an extensively researched one [8, 10]. In addition to exhibiting a relatively high energy conversion efficiency, many silicides are inexpensive, non-toxic and thermodynamically and mechanically stable [8]. This makes them an attractive group of materials for environmentally friendly energy technology.

For high temperature applications such as radioisotope thermoelectric generators used in spacecraft [11], SiGe has proven to be a good material for TEGs with a maximum efficiency of 10% in the temperature range of 300-1200 K [12]. Decreasing thermal conductivity through nanostructuring has also been proven to improve the ZT of both p- and n-type $Si_{1-x}Ge_x$ [13][14]

Magnesium silicide (Mg_2Si) is another well known and extensively researched TE material [10]. In 2005, Tani et. al measured a ZT of 0.86 at 862 K for spark plasma sintering fabricated Mg_2Si doped with 2 at.% bismuth. Nanostructuring was also attempted in the case of Mg_2Si, however, the reduction in thermal conductivity was accompanied by a comparative reduction in the electric conductivity due to similarities in the phononic and electronic mean free path. The resulting reduction in the power factor meant that nanostructuring was not found to be a good solution for this material [15]. This example is illustrative of some of the challenges in tuning of materials properties, as changes in structure or composition can often have unforeseen and unwanted consequences. One other challenge with Mg_2Si is its proclivity for oxidation, along with many of the other group 1 and 2 silicides [8].

Other strategies for improving the efficiency of Mg_2Si, such as alloying and doping have been adopted instead of nanostructuring. As early as 1962, LaBatz et. al showed that the thermal conductivity of Mg_2Si could be reduced by alloying with Ge without increasing the electrical resistivity [16]. An approach of co-doping with Ge and Sb was also able to increase the maximum zT value to 0.74 at 756 K for n-type Mg_2Si compared to a maximum of ~ 0.16 for the undoped sample due to a combination of increased carrier concentration and reduced lattice thermal conductivity.

Many transition metal silicides have also shown promise as TE materials. Of the binary transition metal silicides Cr, Mo, W, Mn, Re, Fe, Ru and Os compounds all tend to be semiconductors usable as TE materials [8].

Manganese silicide, $MnSi_x$ ($1.71 \leq x \leq 1.75$), also known as higher manganese silicide (HMS), has, along with $\beta-FeSi_2$, shown high positive Seebeck coefficients of 150-200 µV/K, making these materials highly promising p-type candidates for TE [8]. Although the ZT of these materials is less than 1, their non-toxicity, chemical and thermal stability as well as being made up of inexpensive, relatively abundant elements, help increase interest in them [17]. $MnSi_x$ (HMS) compounds can be described by several compositions, making up approximately the same M:Si ratio. The phases

form complex chimney-ladder structures with tetragonal cells, which exhibit a distinct anisotropy in electrical conductivity and Seebeck coefficient . First principles pseudopotential calculations on Mn_4Si_7 calculated Seebeck coefficients approaching $\sim 220\,\mu V\,K^{-1}$ at 800 K, both in the [100] and [001] crystallographic directions, with S_a being about $5\,\mu V\,K^{-1}$ higher than S_c [17].

As was also the case for Mg_2Si, partial Ge substitution of Si in HMS lead to an increase in zT by more than 30% relative to the pure HMS resulting in a zT of 0.6 at 575 K [18]. This effect was due to an increase in cell parameters and number of defects, tuning the electrical and thermal properties of the material. A similar result was found for Al substitution of Si. Increasing the number of charge carriers and defects drastically improved the electrical conductivity while decreasing the thermal conductivity, resulting in a zT of 0.65 at 527 °C [19].

$CrSi_2$ is a p-type semiconductor recognized as a potential thermoelectric material for mid-temperature applications due to its high power factor and thermal stability. Unfortunately, $CrSi_2$ also has a very high room temperature thermal conductivity, which severely limits its ZT to around 0.18 [20]. Several attempts have been made at reducing the thermal conductivity. As an example, Upadhyay et. al. managed to achieve an increase of zT to ~ 0.32 at 673 K by adding SiGe nanoinclusions which provided increased phonon scattering [21].

The orthorombic low-temperature β-phase of $FeSi_2$ is a semiconductor of interest for thermoelectric applications. Pure β-$FeSi_2$ is an n-type semiconductor with a band gap of 0.84 ± 0.1 eV [10], that can be doped both to n- and p-type, depending on the chosen dopant elements. The maximum zT reported for Co-doped n-type $Fe_{0.95}Co_{0.05}Si_2$ is 0.4 at 850 K. For Al-doped p-type $FeSi_{1.92}Al_{0.08}$, at the same temperature, the reported zT is 0.2 [10].

All silicides discussed so far have had a Si:M ratio higher than 1, but in 2007, Sakai et. al. conducted a stydy into the thermoelectric power of transition metal monosilicides, looking into $CrSi$–$MnSi$–$FeSi$–$CoSi$–$Co_{0.85}Ni_{0.15}Si$ and their interpolating solid solutions [22]. This study found drastically changing Seebeck coefficients in FeSi at very low temperatures from $-20\,\mu V\,K^{-1}$ at 100 K to $550\,\mu V\,K^{-1}$ at 50 K and back down again to $80\,\mu V\,K^{-1}$ at 5 K. A Seebeck coefficient of $60\,\mu V\,K^{-1}$ at room temperature was also documented for $Fe_{0.2}Co_{0.8}Si$ which, combined with a low electrical resistivity of $\sim 300\,\mu\Omega$ cm gives a promising power factor. Unfortunately, a large thermal conductivity limits the room temperature zT to around 0.1.

1.2.2   High Entropy Alloys

A high entropy alloy (HEA) is a multi-component alloy where configurational entropy is assumed to have a stabilizing effect on the formation of single-phase solid solutions. This rationale can be expressed via the Gibbs energy

$$G = H - TS \qquad (1.2)$$

Where a low (negative) Gibbs energy indicates phase stability and a high configurational entropy (especially at higher temperatures) is thought to counteract the effect of the mixing enthalpies of the elements which would often favor simpler phases. The actual magnitude of the stabilizing entropy effect is open to some discussion [23], but in any case a HEA is an alloy with an appreciable amount of configurational entropy.

Intuition might point to a mixing of many different elements creating brittle samples with complex microstructures. In reality the mixing entropy can in some cases enhance the mutual solubility among the constituent elements and reduce the number of phases[24].

There are two main definitions of what kind of phase can qualify as a HEA:

- Alloys containing at least five principal elements, where $5 \leq$ at% ≤ 35 for each of the principal elements.

- Alloys with a configurational entropy $\Delta S_{conf} \geq 1.5R$, where R is the ideal gas constant.

There is some disagreement in the HEA research field on whether an alloy must be single-phase to be considered a HEA, but in this thesis, a HEA will be taken to mean any single-phased disordered solid solution phase that meets one or both of the above definitions. These requirements are also not necessarily set in stone. For example, the quaternary equimolar CoCrFeNi alloy is close to the lower limits of both requirements without meeting any of them completely, however this compound is also sometimes considered a HEA in literature [25].

Solid solution HEAs often take relatively simple structures, like fcc or bcc, although they have also been known to adopt other structure types, like orthorombic [24, p.44]. If there is ordering of the elements, more complex super cells can form, but it can be discussed whether or not these phases should indeed be called HEAs. Figure 1.1 shows the unit cell of a disordered five-element equiatomic HEA unit cell with the cubic close-packed structure.
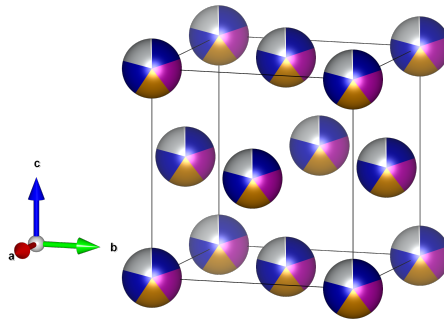

Figure 1.1: The unit cell of a five-element equiatomic HEA adopting the cubic close-packed structure.

The research field of HEAs is a relatively young, but nevertheless prolific one [23, 26]. The vast composition space available through multi-principal element alloys allows for enormous possibilities.

While there are many possibilities for different HEA compositions, the largest volume of research into HEA materials has been centered on 3d-transition metal alloys. Figure 1.2 shows a distribution of elements present in reported HEAs up until 2016, revealing that the vast majority (over 70 %) of examined alloys contain at least one (usually more) of the following elements: Cr, Fe, Co and Ni.
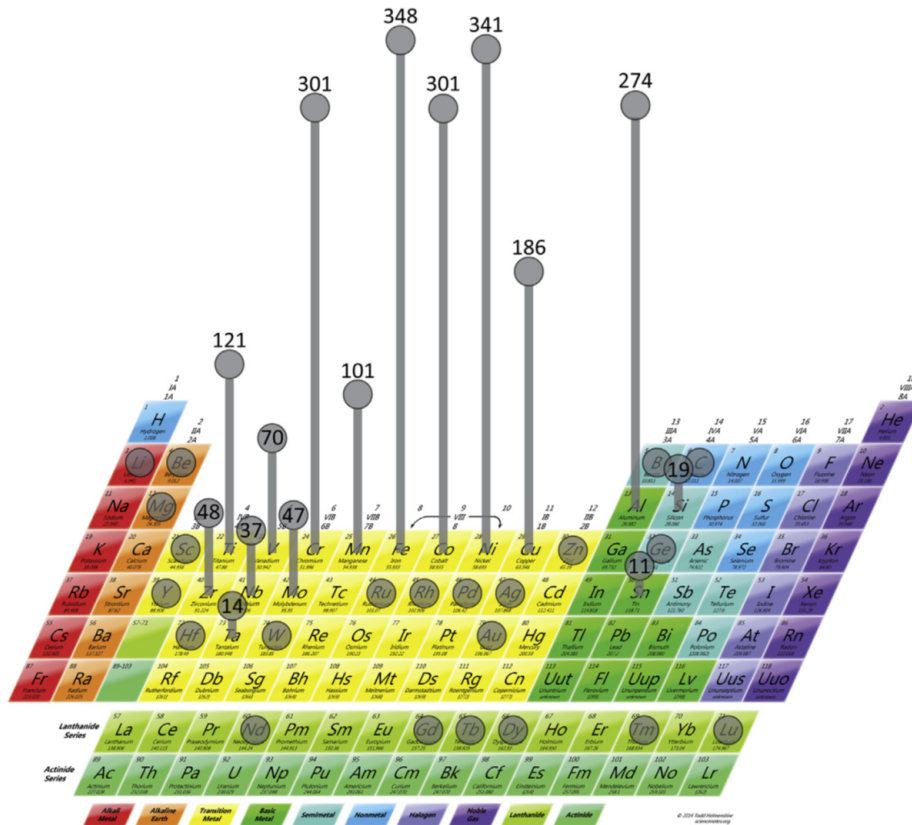
Figure 1.2: Illustration of the distribution of different elements in reported high entropy alloys up until 2016. Figure copied from [23]

The earliest results on crystalline HEAs or multi-principal element alloy (MPEA)s were reported by Cantor et.al. in 2004 on several equiatomic alloys, including the equiatomic five-component $Fe_{20}Cr_{20}Mn_{20}Ni_{20}Co_{20}$ alloy, often referred to as the Cantor alloy [27]. In the study, this alloy was found to form a single-phase FCC solid solution. The study also found that a wide range of other six- to nine-element alloys made from the late transition metal elements created similar FCC-structures which could dissolve substantial amounts of other transition metals like Nb, Ti and V. More electronegative metals like Cu and Ge were not found to dissolve easily into these alloys, and instead were shown to segregate into the interdendritic regions.

Disordered FCC structures are by far the most common reported for metallic alloys, found 465 times in 410 alloys, followed by BCC (357 times in 306 alloys). Ordered intermetallic phases, hexagonal high-entropy phases and other structure types are also found, but these are less common [23]. Whether the reason for this structure distribution lies in the elements most often used in HEAs or somewhere else was unclear.

The vast majority of research into the HEA and MPEA field is centered on the structural and microstructural properties of the alloys. Less focus has gone into functional properties, and specifically possible thermoelectric properties, but a few studies have dealt with these areas as well. In a 2013 review article, Tsai et al. found that, in general, HEAs had electrical resistivities that were 1-2 orders of magnitude higher than pure metals but only slightly higher than conventional alloys [9]. The thermal conductivity was generally found to be notably lower than pure metals, but about the same as for conventional alloys. Common for both the electrical and thermal conductivity, however, was that these properties generally displayed a lower temperature dependency in HEAs relative to conventional alloys. This can be explained bu the lattice distortion caused bu thermal vibrations being relatively small compared with the lattice distortion already found in many HEAs

due to size differences in solute atoms [24, p.59].

Very few studies have introduced silicon into HEA structures, but in 2020, Babilas et. al. examined the effect of chromium and silicon content on AlCoCrFeNiSi high entropy alloys [28]. They found that the addition of silicon and chromium strongly affected the structures of the alloys, with new crystallographic phases being formed. A different study performed in 2019 by Niu et. al. found that addition of silicon to the HEA (AlCrTiZrV)N thin films lead to a structure change from a simple fcc to a bcc structure [29]. Low intensity XRD peaks also indicated a change in the microstructure with the addition of silicon to a nanocrystalline or amorphous phase.

Interesting microstructures are often found in high entropy alloy systems. In 2016, Jensen et. al. observed a remarkable periodic two-phase microstructure, consisting of a disordered bcc phase which was aligned orthogonally within a matrix of an ordered B2 phase in the $Al_1Mo_{0.5}Nb_1Ta_{0.5}Ti_1Zr_1$ [30]. In a different study by Tsai et. al. published in 2009, a microstructure containing Widmanstätten Cu-rich precipitates and a low stacking fault energy in the material prompted the nucleation of nanotwins in the structure [31].

Chapter 2

Theory

In this chapter an attempt will be made to lay the theoretical foundation for the methods and arguments presented in this thesis.

2.1 Thermoelectricity

The thermoelectric effects describe the occurrence of electric field gradients within a material in response to a thermal gradient, and *vice versa*.

2.1.1 Seebeck Effect

The Seebeck effect was first discovered by Thomas Johann Seebeck as early as 1821, when he discovered that a compass needle was deflected by a closed loop of two dissimilar conductors when one of the junctions were subjected to heat [32, p. 23]. The Seebeck effect describes a voltage that is produced as a response to a temperature gradient across any isolated conducting material [32, p.1-2]. The magnitude of this effect is described by the Seebeck coefficient:

$$S = \frac{V}{\Delta T} \tag{2.1}$$

A positive (negative) Seebeck coefficient indicates holes (electrons) as the majority charge carrier and the absolute value of S is often referred to as thermopower. Metallic materials have a low S of only a few $\mu V\,K^{-1}$, while good thermoelectric materials show higher values between 200 and 400 $\mu V\,K^{-1}$.

2.1.2 Peltier Effect

The Peltier effect is also known as the reverse thermoelectric effect. When charges move across a junction between two dissimilar conductors (or semiconductors), there is a small change in heat at the junction due to the change in the entropy of the electrical charge carriers from one material to the other. Figure 2.1 shows a closed loop circuit consisting of Fe and Cu. In the junction where current flows from the Cu to the Fe conductor, heat is absorbed by the charge carriers, and the temperature of the junction is lowered. At the junction where the charge carriers move from the Fe to the Cu, heat is released, and the temperature at the junction rises.
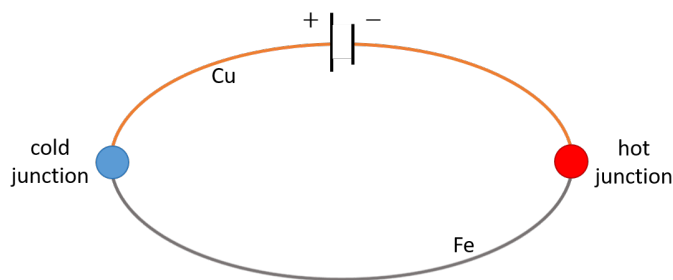
Figure 2.1: A closed loop circuit consisting of iron and copper displaying the Peltier effect with cooling at one junction and heating at the other. If the direction of the current is reversed, the heating/cooling effect will also be reversed, and the cold and hot junctions will switch places.

The magnitude of the Peltier effect is described by the Peltier coefficient, Π_{ab}, as demonstrated in equation 2.2

$$\Pi_{ab} = \frac{Q}{I} \tag{2.2}$$

2.1.3 Thermoelectric generator

A thermoelectric generator (TEG) is made up of pairs of p-and n-doped semiconductors that are connected electrically in series and thermally in parallel. As the Seebeck coefficient of the p- and n-doped legs is, respectively, positive and negative, the individual voltages will add up and the TEG produces a sizeable output voltage, when subjected to a temperature gradient. This effect is illustrated in Figure 2.2
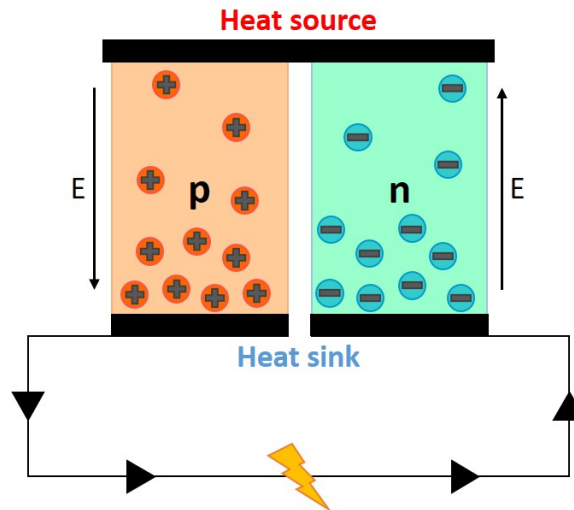

Figure 2.2: Schematic illustration of a TEG. When subjected to a heat gradient, the majority charge carriers in the n-and p-type legs will migrate towards the colder side, giving rise to a voltage.

If a thermoelectric generator is instead connected to a power source, the reverse thermoelectric effect (Peltier effect) will instead create a temperature gradient. In this case, it is called a Peltier element, and this can be used for thermoelectric heating or cooling.

2.1.4 Thermoelectric Figure of Merit

The thermoelectric figure of merit, zT, is closely related to the efficiency with which a thermoelectric material can convert thermal energy into electric energy. It is defined as

$$zT = \frac{\sigma S^2 T}{\kappa} \tag{2.3}$$

where σ ia the electrical conductivity, S is the Seebeck coefficient, T is the temperature in Kelvin and κ is the thermal conductivity. The ZT of a TEG is found by taking the average of the zTs of the two TE materials making up the TEG. As all of the factors making up the figure of merit are at least somewhat temperature dependent (not least the temperature itself), there are complex interactions to take into consideration when attempting to influence its value. Another factor to consider is that thermoelectric materials must work in n-p-pairs in a TEG. The zT for both materials should therefore ideally have their highest values at approximately the same temperature.

2.2 Crystallography

The atomic structure of a crystalline solid is an important decider of both the mechanichal and functional properties of that solid. For this reason, crystallography is a vital part of materials characterization.

2.2.1 The crystal lattice

A crystal is a periodic array of atoms, classified by a specific set of symmetry operations. All three-dimensional crystal structures can be sorted into one of 14 different types of Bravais lattices. The bravais lattices are sorted by crystal system (cubic, hexagonal, orthorombic, etc.) and type of centering (primitive, face-centered, body-centered, etc.).

    The unit cell of a crystal is the smallest possible collection of lattice points that, when repeated in all three dimensions, captures the full symmetry of the crystal. A unit cell is described by its type of Bravais lattice, along with the unit vectors ($\mathbf{a}$, $\mathbf{b}$ and $\mathbf{c}$) spanning the cell and a basis of atoms. It is worth specifying the difference between an atom and a lattice point. A lattice point is a mathematical point in space, representing a basis of atoms. As an example, the cesium chloride (CsCl) crystal has a primitive cubic Bravais lattice, which consists of only one lattice point (each corner point counts as $1/8 \Rightarrow 8 \times 1/8 = 1$). However, the CsCl basis consists of two ions: one Cs^+ and one Cl^-, so while the unit cell contains only one lattice point, it contains two atoms. Figure 2.3 shows a primitive cubic unit cell of cesium chloride.
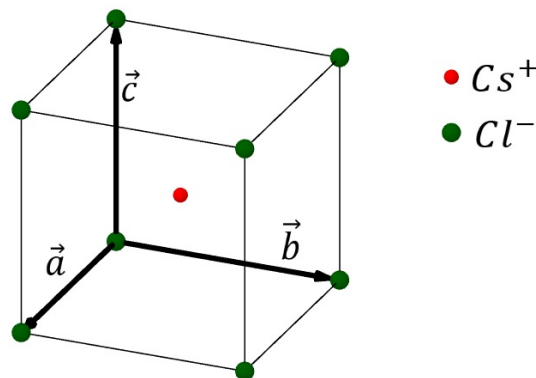

Figure 2.3: Primitive cubic unit cell of CsCl. Unit vectors $\mathbf{a}$, $\mathbf{b}$ and $\mathbf{c}$ spanning the cell. Primitive unit cells contain —point. The CsCl basis consists of two atoms, so the unit cell contains two atoms.

2.2.2 The reciprocal lattice

The reciprocal lattice is a Fourier transform of the crystal lattice from real space in to reciprocal space. The reciprocal lattice vectors ($\mathbf{a}^*$, $\mathbf{b}^*$ and $\mathbf{c}^*$) can be constructed from the real lattice vectors as shown in eq. 2.4:

$$\mathbf{a}^* = 2\pi \frac{\mathbf{b} \times \mathbf{c}}{\mathbf{a} \cdot \mathbf{b} \times \mathbf{c}} \quad \mathbf{b}^* = 2\pi \frac{\mathbf{c} \times \mathbf{a}}{\mathbf{a} \cdot \mathbf{b} \times \mathbf{c}} \quad \mathbf{c}^* = 2\pi \frac{\mathbf{a} \times \mathbf{b}}{\mathbf{a} \cdot \mathbf{b} \times \mathbf{c}} \tag{2.4}$$

    There are several reasons why the reciprocal lattice of a crystal is worth investigating. Electrons in a crystal are often described by their wave vector $\mathbf{k}$, which is found in reciprocal space, as are phonons, which are quantized lattice vibrations that play a key role in thermal conduction. The first Brillouin zone of the reciprocal lattice is an analogue to the primitive unit cell of the real crystal, in that all wavevectors in the crystal can be represented within the first Brillouin Zone.

One of the most important tools in structure determination is diffraction experiments. These experiments give us information about the reciprocal lattice, which can then be interpreted to give information regarding the real lattice.

2.2.3 Diffraction

The general meaning of the word diffraction is the spreading or bending of waves around obstacles. In crystallography, diffraction of X-rays, electrons or neutrons in a crystal is a commonly used method for structure determination. One simple condition for diffraction from a specific set of crystal planes is described by Bragg's law

$$2\mathrm{d}sin\Theta = n\lambda \tag{2.5}$$

Where λ is the wavelength of the incoming wave, Θ is the angle between the incoming wave and the set of planes, d is the distance between the planes, and n is an integer. Figure 2.4 illustrates the Bragg condition for diffraction. In the figure, two incoming waves are reflected off subsequent atomic planes in a crystal. If the path difference experienced by the second beam is equal to a whole integer multiple of its wavelength, the two beams will emerge from the crystal in phase, and interfere constructively, and the condition for diffraction is fulfilled.
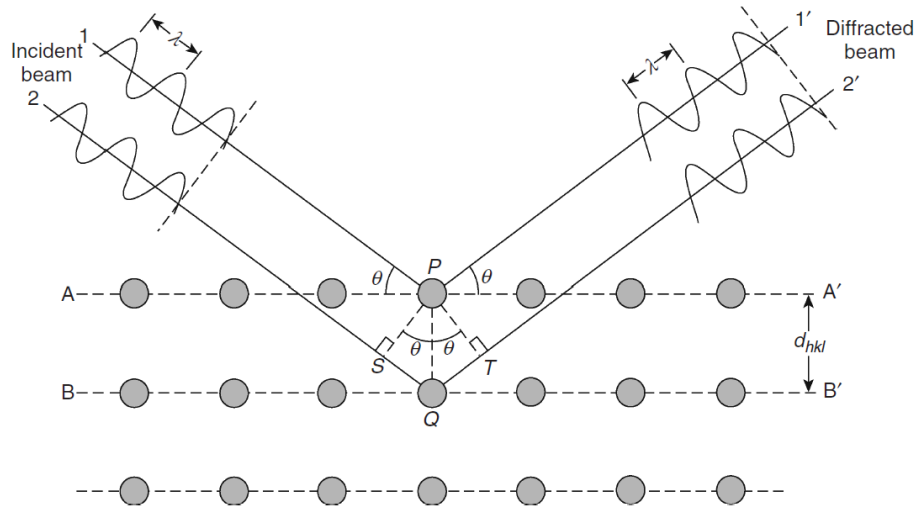

Figure 2.4: Bragg condition for diffraction by crystal planes. If the path difference between the two beams $SQ + QT = 2d_{hkl}sin\theta$ is equal to $n\lambda$, where n is an integer, the emerging beams will interfere constructively and the condition for diffraction is fulfilled. Figure copied from [33]

The Laue condition looks at the diffraction phenomenon in reciprocal space. Here, we consider the incoming wave vector $\mathbf{k}$ and the outgoing wave vector $\mathbf{k}'$. The Laue Condition for diffraction simply states that if the change in wavevector $\Delta\mathbf{k}$ is equal to a reciprocal lattice vector, diffraction will occur. This condition is summed up in equation 2.6

$$\Delta\mathbf{k} = \mathbf{k}' - \mathbf{k} = \mathbf{G} \tag{2.6}$$

where $\mathbf{G}$ is a reciprocal lattice vector (i.e. any linear combination of the primitive reciprocal lattice vectors $\mathbf{a}^*, \mathbf{b}^*$ and $\mathbf{c}^*$).

2.3 Electric conductivity

The electrical conductivity, σ, can be defined as in equation 2.7

$$\sigma = \frac{\mathbf{j}}{\mathbf{E}} \tag{2.7}$$

where $\mathbf{j}$ is the electrical current density and $\mathbf{E}$ is the electric field strength. Simply stated: the electrical conductivity can be described as the current density response to the influence of an electric field. The simplest explanation of electrical conductivity is given by the free electron Fermi gas model.

In reciprocal space, the momentum, $\mathbf{p}$ of an electron (free or in a crystal) is related to its wavevector, $\mathbf{k}$, by the relation in equation 2.8

$$\mathbf{p} = m\mathbf{v} = \hbar\mathbf{k} \tag{2.8}$$

where m is the mass of the electron (in a crystal, the effective mass of the electron is dependent on the periodic potential), and $\mathbf{v}$ is the velocity with which the electron travels. In their ground state, all electrons in a crystal are in their lowest available energy states. In reciprocal space, these energy states make up the Fermi sphere, where the surface of this sphere makes up the Fermi level (or Fermi surface).

Under the influence of an electric field in the steady state, the entire Fermi sphere is shifted by

$$\delta\mathbf{k} = -e\mathbf{E}\tau/\hbar \tag{2.9}$$

where e is the electron charge and τ is the average time between collisions caused by lattice impurities, imperfections or phonons. By combining 2.8 and 2.9 we get that the electron velocity as a result of an electric field is given by

$$\mathbf{v} = \frac{\delta\mathbf{k}}{m} = \frac{-e\mathbf{E}\tau}{m}. \tag{2.10}$$

The electronic current density in a constant electric field with n electrons per unit volume is then given by Ohms law:

$$\mathbf{j} = -ne\mathbf{v} = \frac{ne^2\tau\mathbf{E}}{m}. \tag{2.11}$$

From the definition of electrical conductivity given in 2.7, we then get a new expression for the conductivity, given by equation 2.12

$$\sigma = \frac{ne^2\tau}{m}. \tag{2.12}$$

From 2.12, we can see that the electrical conductivity is proportional with the number of charge carriers and the mean time between collisions, and inversely proportional with the mass (or effective mass) of the electron. A good electrical conductor should then have a high concentration of charge carriers with a small effective mass (weakly bound), and few scattering centers (lattice imperfections, impurities and phonons).

2.4   Thermal conductivity

The thermal conductivity κ of a material is defined as the heat flux Q through a unit area of the material as a function of a temperature gradient, as shown in equation 2.13.

$$\kappa = -\frac{Q}{\nabla T} \tag{2.13}$$

The thermal conductivity can be split into two parts, the electronic thermal conductivity κ_e and the lattice thermal conductivity κ_l. The total thermal conductivity is the sum of these two contributions

$$\kappa = \kappa_e + \kappa_l \tag{2.14}$$

The electronic contribution can be defined as

$$\kappa_e = \left(\frac{k_B}{e}\right)^2 L_0 \sigma T \tag{2.15}$$

where k_B is the Boltzmann constant, e is the elementary charge, L_0 is the Lorentz number, σ is the electrical conductivity, and T is the temperature in Kelvin [32, ch.2.5.1].

Since κ_e is directly proportional to σ, any attempt at tuning of κ for thermoelectric purposes is therefore focused around changing the value of κ_l

The lattice contribution to the thermal conductivity is due to phonons. A phonon is a quasiparticle describing quantized lattice vibrations. The energy of a phonon is related to the vibrational amplitude and frequency of the atoms in a lattice.

In order to visualize this, one can imagine a one-dimensional chain of identical atoms, connected by springs. The stronger the oscillations of the atoms, the more energy is transferred through the springs.

In non-metals the lattice thermal conductivity term dominates over the electronic conductivity term. Lattice vibrations are the primary mechanism by which thermal energy is transported.

The kinetic theory of gases leads to an expression that, analogously, can be used for a phonon gas.

$$\kappa = \frac{1}{3}Cv\ell \tag{2.16}$$

Where C is the volumetric heat capacity, v is the mean phonon velocity and ℓ is the phonon mean free path. The mean free path is determined mainly by two different processes, geometrical scattering and inter-phonon collisions. In geometrical scattering it is grain boundaries and other defects that make it hard for phonons to travel uninhibited through the crystal, but this occurs primarily at very low temperatures. The phonons can also scatter by colliding with other phonons, but only inelastic collisions (those in which momentum is not conserved) contributes to changing the overall thermal conductivity. This happens in umklapp processes

$$\mathbf{k}_1 + \mathbf{k}_2 = \mathbf{k}_3 + \mathbf{G} \tag{2.17}$$

Where the sum of initial phonon wavevectors extends the Brillouin Zone and the wavevector of the outgoing phonon is brought back into the Brillouin Zone. These processes occur more frequently at higher temperatures when the phonons have more energy.

Chapter 3

Methods

3.1   Specimen Synthesis

All bulk specimens used in this project were prepared by arc melting and provided by Patricia Carvalho, one of my supervisors on the project and the project leader on our main project, ANSWER. The initial set of specimens, i.e. M_2Si-1.0 and M_2Si-1.1 were prepared in Portugal by colleagues of her, and the subsequent specimens were prepared at SINTEF in Oslo on the arc melter in their lab.

Three different bulk specimens were prepared for this project, and most of these have been examined both in their as cast state and after annealing in quartz tube under partial vacuum at different temperatures and times. The main focus has nevertheless been on understanding the phases and microstructure of the M_2Si-1.1 specimen after annealing. An overview of the specimens examined in this thesis can be seen in table 3.1

Table 3.1: Bulk sample nominal composition overview.

Sample name	Nominal Composition	Comment
M_2Si-1.0a	$Si_{33}Cr_{13}Fe_{13}Co_{13}Ni_{13}Cu_{13}$	As cast
M_2Si-1.0b	Same as above	Annealed at 800°C for 8 hrs
M_2Si-1.1	$Si_{33}Cr_{17}Fe_{17}Co_{17}Ni_{17}$	Annealed at 900°C for 40 hrs
M_2Si-1.2a	$Si_{32}Cr_{16}Fe_{19}Co_{18}Ni_{15}$	As cast
M_2Si-1.2b	Same as above	Annealed at 900°C for 42 hrs

3.2   Sample Preparation

Powder samples for initial TEM experiments on M_2Si were prepared by fine crushing in a mortar along with isopropanol and depositing suspended particles on holey carbon Cu grids. Because of the Cu content in the material, a powdered sample was also deposited on a gold grid to allow for easier composition determination using EDS.

Attempts were made to gain an overview over the different compositions/phases present in the powder TEM samples prepared. These results are summarized in table 8.1 in chapter 8. However, a high degree of variation in measured compositions, as well as a proclivity for oxidation and beam sensitivity in many of the grains in the powder samples, lead to the decision to focus efforts on bulk TEM samples instead. Some particles could be observed undergoing rapid phase changes under the illumination of the electron beam, making prolonged study of any single particle challenging. An example of this behavior can be observed in Figure 8.1 in chapter 8.

Bulk TEM samples of the M2Si were prepared by cutting appropriately sized pieces from the arc melted bulk samples using a TechCut 4™and ground down to about 15 µm using a Multi-Prep™with diamond lapping paper. Further thinning was done in a PIPSII™ion mill.

Samples for powder XRD were prepared by crushing a cut piece of the bulk sample in a mortar into a fine powder and mixing the powder with a small amount of Si NIST 640 d standard for calibration of results.

3.3 Instrumentation

All SEM experiments for this thesis were performed on polished bulk samples by Patricia Carvalho in the lab at SINTEF on their FEI NANOLAB 600 SEM with an Oxford Instruments EDS. The reason for this was because the SEM in our research group did not have the contrast and spatial resolution necessary to properly examine the phase compositions and microstructure of the samples examined in this project, and I was not allowed in any of the labs at SINTEF due to Covid-19 restrictions.

Measurements of bulk sample resistivity and Seebeck coefficient were performed by Matthias Schrade at SINTEF for the same reasons as mentioned above. Both sets of measurements were performed in-plane in an inert N_2 atmosphere, using the instrumentation described in [34].

XRD experiments were performed on a Rigaku MiniFlex 600 tabletop XRD with a Cu K_α X-ray source. Fitting of spectra and identification of possible structure matches was done using the diffrac.EVA software and cell parameters were refined with the UnitCell software. XRD results and comparisons with simulated diffractograms were plotted using Excel.

Initial TEM imaging and diffraction experiments were performed on a JEM2100F TEM at 200 kV. A combination of STEM imaging, EDS maps and SAED was used to aid in identifying the different phases and structures.
A FEI Titan G2 60-300 TEM was used at 300 kV to obtain higher quality EDS maps and some high resolution STEM images, as well as some further SAED patterns.

3.4 Simulations for comparisons with experimental data

VESTA has been used with .cif-files found through ICSD for simulations of crystal structures and calculated X-ray diffractograms.
The SingleCrystal software has been used together with data gathered from the ICSD .cif-files together with experimental data from XRD and EDS to create suggestions for .cif-files for some of the examined HEA phases.
Simulation of SAED patterns has been done using the JEMS software together with .cif-files tuned with the lattice constants obtained from XRD data.
The simulated X-ray diffractograms were calculated using .cif-files aquired from the ICSD database and tuned lattice parameters from the XRD patterns in the Vesta powder diffraction simulation function.

3.5   Experimental Methods

3.5.1   Electron Microscopy

The study of materials on an atomic level requires powerful microscopes with resolutions far beyond that of the human eye. Even the best visible light microscope (VLM)s available are constrained by the wavelength of visible light, such that the best resolution that can be expected from a VLM is around 300 nm, which corresponds to about 1000 atom diameters [35]. As the DeBroglie wavelength of an electron is dependent on its kinetic energy, this wavelength constraint can be avoided by using electrons accelerated by high voltages. This is the principle behind electron microscopes.

The types of electron microscope in use today can be divided into SEMs and TEMs. A SEM is a scanning electron microscope, while a TEM is a transmission electron microscope. The main difference between the two methods lie in their names; in a SEM, the beam is scanned across the sample and reflected onto a set of detectors, while in a transmission electron microscope (TEM), the beam is transmitted through a very thin sample onto a detector. The achievable spatial resolution of a SEM is usually on the order of $10^{-7} - 10^{-9}$m, while a monochromated and aberration-corrected TEM can achieve resolutions in the sub-Ångstrom range [36]. Partly because of the superior resolution possible when using electrons, TEM and SEM are some of the most widely used tools for examination of materials on a nano and atomic level.

The part of the instrumentation which creates the high-energy beam of electrons is called the electron gun. This consists of an electron source and an acceleration voltage. The different types of electron sources can be divided into thermionic and field-emission sources. Thermionic electron sources are often made of tungsten or lanthanum hexaborate (LaB_6) and their operational principle is based on heating up the material enough that sufficient energy is provided to the electrons in the material to overcome their work function, Φ, and be released from the surface. Field-emission sources (also called FEGs or field-emission guns) can be split into Schottky FEGs and cold FEGs. Field-emission sources operate on the principle that a strong electric field experienced by the tip of the electron source, "rips" electrons from the material.

Regardless of source; after the electrons are freed from their source material, they are subjected to a high voltage. In SEMs, this is usually on the order of 1-40 kV, while in a TEM normal acceleration voltages range from 60-300 kV. This voltage accelerates the electrons, increasing their kinetic energy and decreasing their deBroglie wavelengths to a few pm. Field-emission sources are generally brighter and produce less energy spread in the electron beam, so high-end electron microscopes usually use FEGs.

The optics in electron microscopes are very different from in an optical microscope. Since electrons are not deflected in the same ways as photons in optical lenses, electromagnetic force fields are used to guide the beam paths of electrons through the microscopes. These electromagnetic lenses are made of solenoids surrounding the beam path of the electrons. By running a current through the wires in the solenoid, a strong magnetic field is generated, and this field bends the paths of the electrons. By varying the current through the wires, the strength of the lenses can be controlled.

SEM

Figure 3.1 shows a schematic illustration of a SEM. The electron gun is found at the top of the microscope, followed by a set of condenser lenses. The purpose of these condenser lenses is to reduce the crossover diameter of the beam that enters the objective lens. The objective lens then focuses the beam to a spot on the sample surface. A beam-deflector system then causes the beam to scan across the surface of the sample. A detector outside the optical path in the column then registers the intensity acquired for each scanned point, with each scanning point corresponding to

one pixel of the final image. These intensities are amplified and subsequently assembled together to form the image.
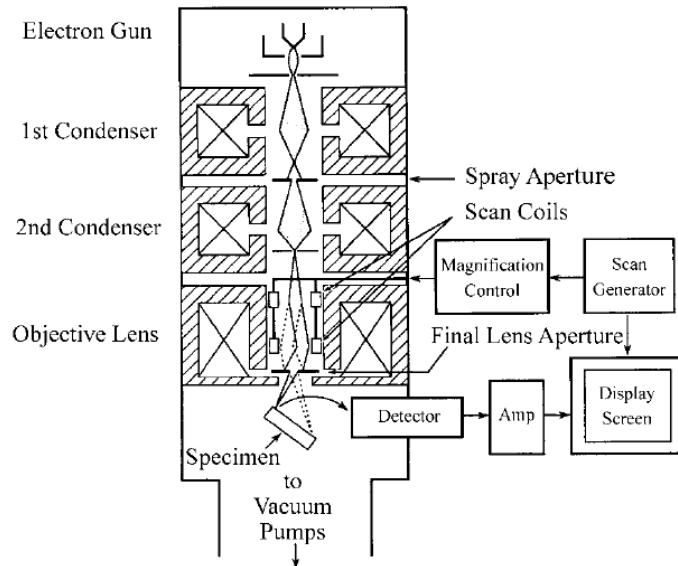

Figure 3.1: Schematic illustration of a SEM. After the electron beam is produced and accelerated by an electron gun, it is sent through a set of condenser lenses which reduce the crossover diameter of the beam before it enters the objective lens. The objective lens then further reduces the diameter of the beam and focuses it to a spot with a diameter in the nanometer range. A deflection system scans the beam across the sample surface, and the intensity in each scanned pixel is then detected and amplified, before being assembled together to form an image. Figure copied from [33]

There are two main types of electron detectors used for imaging in a SEM. These are back-scattered electrons (BSE) detectors and secondary electron (SE) detectors. BSE images are made from the electrons which are elastically scattered in the sample, and the contrast gained from these kinds of images is primarily dependent on the atomic masses of the elements in the sample. Heavier elements scatter electrons more strongly, and so areas of the sample containing heavier elements will appear brighter in a BSE image. SE images are made up of inelastically scattered electrons. These electrons have lost energy through interactions with the sample electrons, and can escape from a much shallower and smaller volume of the sample. The contrast in SE images is for this reason primarily topographical. As a result of the lower energy and consequently smaller interaction volume when using secondary electrons for imaging, a higher spatial resolution can be achieved when recording SE relative to BSE images. The choice between imaging detectors in the SEM therefore depends on whether spatial resolution or mass constrast is most beneficial for your specific needs.

SEM samples can take many different forms, such as bulk materials, powders or thin films, which makes this method very versatile and simplifies the experimental process. SEMs can also be used for several purposes in addition to imaging. Spectroscopy and diffraction experiments can also be performed in an SEM, depending on the types of detectors present in the microscope. Of these, EDS is perhaps one of the most commonly used, but this method will be explained in more detail in section 3.5.3.

3.5.2   TEM

One main difference between a SEM and a TEM is the types of samples used. In a TEM, the beam must pass through the sample in order for an image to be created. In other words, the areas of a TEM sample that is to be observed must be very thin, ideally no more than 100 nm.

Figure 3.2 shows a schematic illustration of a TEM in parallel illumination mode, up until the first image plane. In the following, the ray path of the electron beam and the most central parts of the instrumentation will be explained. TEMs can also be operated in so-called STEM-mode, where the incident beam hitting the sample is converged to a point and scanned over the sample, much like in a SEM. A brief explanation of the differences relevant for STEM mode operation will be presented later in this section.
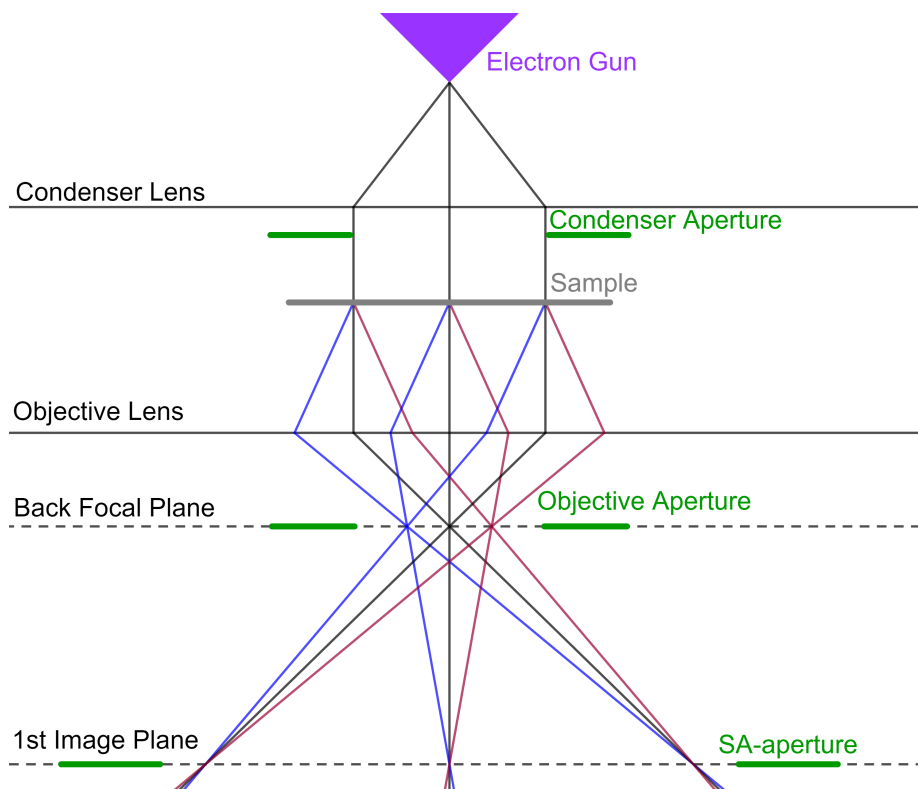

Figure 3.2: Schematic illustration of the beam path taken through the TEM in parallel illumination mode, from the electron gun until it reaches the first image plane.

The first set of lenses in the TEM are the condenser lenses, illustrated as a single lens in Figure 3.2. These lenses control the incident angle of the beam onto the surface of the sample and, depending on their strength, the beam can either be spread out to cover a large area of the sample, or converged into a spot. In TEM imaging, a (close to) parallel beam is used.

The condenser aperture helps control the intensity of the sample by blocking out some of the beam. When imaging sensitive specimens, using a smaller condenser aperture can help with avoiding beam damage to the sample.

When passing through the sample, the incident electrons can get deflected and diffracted in different directions, depending on the structure of the atoms in the sample, as described in section 2.2.3. Inelastic scattering of some of the high-energy incident electrons will also occur, where they transfer some of their energy to electrons in the sample. One of the signals these inelastic scattering events give rise to is the emission of characteristic X-rays from atoms in the sample, which can then be detected by an EDS detector placed in the microscope column and used for chemical analysis.

After the sample, the electron beam passes through the objective lens. This lens is responsible for creating both the primary image of the sample and the diffraction pattern. As can be seen in Figure 3.2, all electrons that are elastically scattered in the same direction in the sample will meet in the back focal plane of the objective lens, creating the diffraction pattern, and all electrons that are scattered from the same point on the sample will meet in the first image plane, creating the image of the sample.

In the back focal plane, the electron diffraction pattern from the sample is found. This diffraction pattern is a representation of a part of the reciprocal lattice of the illuminated part of the sample. In order to understand the representation of the reciprocal lattice that is seen in a TEM diffraction pattern, one can imagine a sphere with radius equal to the length of the wavevector of the incident electrons, as shown in Figure 3.3. This sphere is called the Ewald sphere, and where the surface of this sphere intersects with a reciprocal lattice point, The Laue condition for diffraction is fulfilled, and a diffracted intensity can be observed in the back focal plane. When the Ewald sphere intersects with lattice points from more than one layer of the reciprocal crystal, these are called higher-order Laue Zones. These are very useful in structure characterization as they contain 3-dimensional information about the reciprocal (and by extension, the real) lattice.
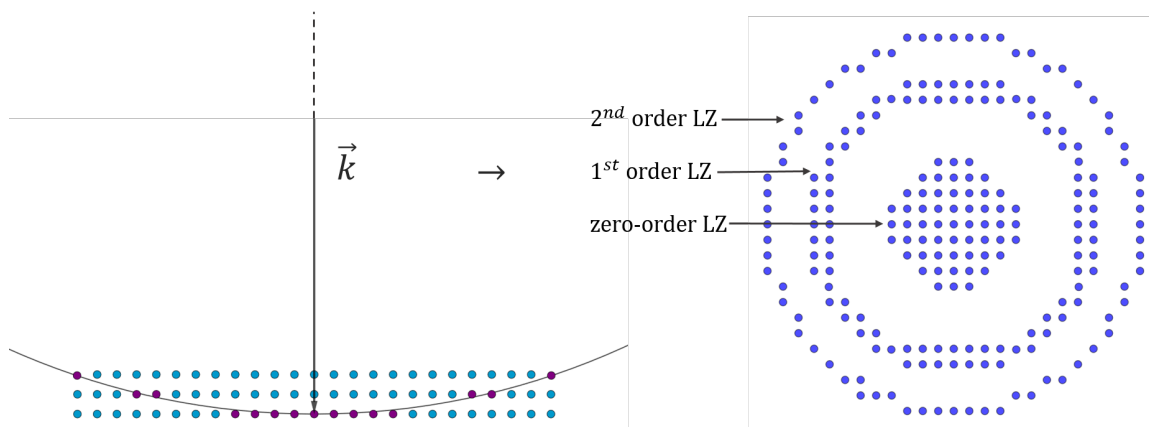

Figure 3.3: Illustration of a cross-section of the surface of the Ewald sphere and the reciprocal lattice. Where the Ewald sphere surface intersects with a reciprocal lattice point, the Laue condition is fulfilled, and a diffracted intensity can be observed in the back focal plane. The observed diffraction pattern in the back focal plane is illustrated to the right. When the Ewald sphere intersects with lattice points from more than one lattice plane, higher-order Laue zone patterns can be observed.

The objective aperture can also be found in the back focal plane of the objective lens. This is used to select specific parts of the diffraction pattern to achieve different types of contrast. In a bright field (BF) image, the objective aperture is placed in a way so as to select only the central beam for imaging. In a BF image, weakly scattering grains will appear bright, while strongly scattering grains will appear dark. In dark field (DF) imaging, the objective aperture is used to block out the central beam, so that only scattered electrons contribute to the image formation. In DF images, strongly scattering grains will appear bright. The differences in contrast made available by the active use of the objective aperture allows us to more easily spot differently oriented grains and defects in the sample.

In the first image plane of the objective lens, the electrons that were scattered from the same point on the sample meet again to form an image. In this plane, the selected area aperture is found. This aperture is used for the purpose of selected area electron diffraction (SAED). By blocking all electrons scattered from other areas of the sample, diffraction information from specific phases or grains can be obtained. This is especially useful for poly-crystalline samples or samples consisting of more than one phase.

After the first image plane, the beam enters the intermediate and projector lens system. The purpose of the intermediate lenses is to control whether the image projected on the camera or fluorescent screen in the bottom of the microscope column should be the diffraction pattern (back focal plane) or the image plane. By changing the strength of the intermediate lens, the TEM can easily switch between diffraction and imaging mode. The purpose of the projector lenses is simply to further enlarge and project the image defined by the intermediate lens onto a camera or fluorescent screen so that it can be observed.

STEM mode

In STEM mode, the condenser lenses are adjusted so that the incident beam is converged to illuminate only a small point on the sample. The beam is then scanned over the sample while detectors register the transmitted beam intensity in each point. These intensities are then combined to create an image, in the same way as in a SEM.

Different STEM detectors pick up electrons scattered at different angles, as illustrated in Figure 3.4. The scattering mechanism is strongly correlated to the scattering angle so the different detectors will give correspondingly different kinds of contrasts as well. BF detectors measure the intensity of the parts of the beam that are scattered at the smallest angles and show mainly diffraction contrast, comparable to a TEM BF image. DF detectors measure the intensity of the parts of the beam that are scattered at larger angles. The HAADF detector recieves the electrons scattered at the largest angles, and these images show so-called Z contrast, which means that the elements with the highest atomic numbers will show up the brightest in HAADF images.
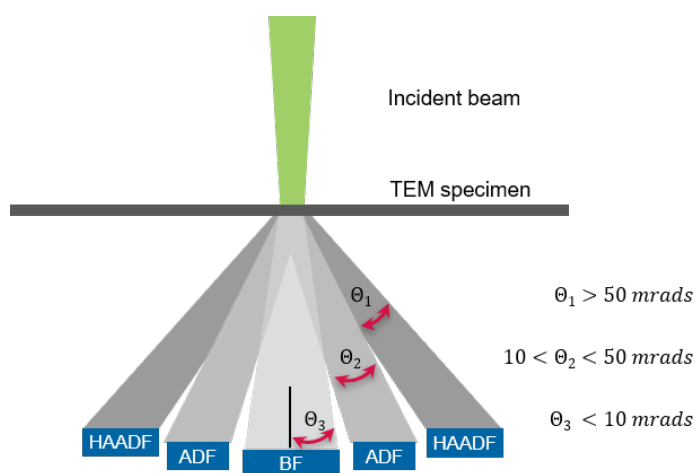

Figure 3.4: Illustration of the various collection angles for BF, ADF and HAADF. Image copied from https://www.gatan.com/techniques/4d-stem.

The detectors have circular symmetry (i.e. annular) in order to collect as much signal as possible at their respective collection angles. Because the collection angles of the different detectors do not overlap, the STEM is capable of sampling with all of them in parallel for a single image.

3.5.3 X-ray Energy Dispersive Spectroscopy (EDS)

EDS is a characterization technique using characteristic X-rays to identify chemical elements in a sample. From the X-rays that are emitted and detected, the specific elements, as well as their relative amounts in a sample can be determined.

By irradiating the sample with high energy electrons in an electron microscope, electrons in the inner shells of the atoms in the sample can be 'kicked out' of their shells, as illustrated in Figure 3.5. This creates an empty lower energy electron state that is quickly filled by an electron from a higher energy shell as the atoms always want to reach their lowest possible energy state. When the hole is filled by a higher energy electron, one of two things can happen: The atom either emits the excess energy as a characteristic X-ray photon, or the energy is used to kick out an outer shell electron (Auger electron).
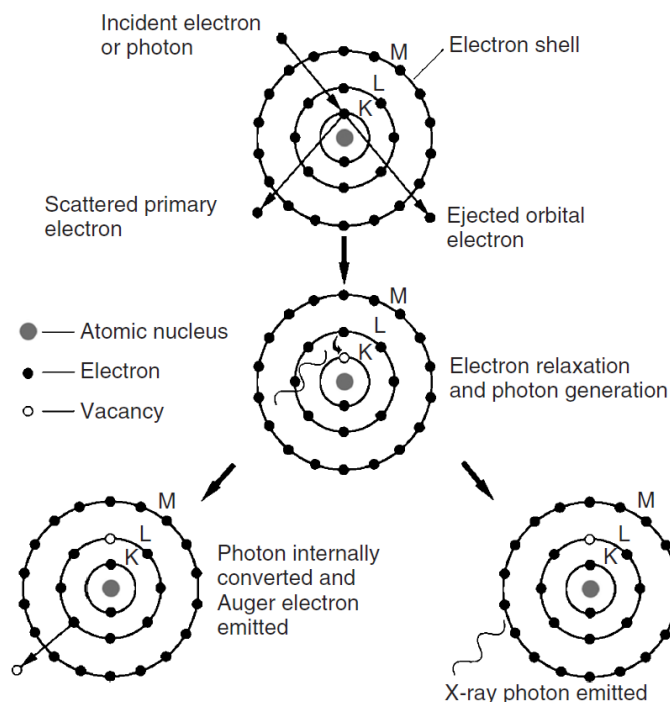

Figure 3.5: Illustration showing a high energy incident electron being scattered by a core electron in an atom and transferring some of its energy to the core electron, causing it to be ejected from its orbital. The figure further shows the two possible processes that can occur upon relaxation of the atom to a lower energy state. The bottom left atom shows the generation of an Auger electron and the bottom right one shows the generation of a characteristic X-ray photon. Figure copied from [33]

The energies of the characteristic X-rays are equal to the energy difference between the initial and final energy states of the relaxing electron. These energies in turn depend on the core charge and electron structure of each atom, and are therefore unique for each element.

The Siegbahn notation is commonly used to specify characteristic X-rays. This comprises of a capital English letter, a lower-case Greek letter, and a subscript number [33, p. 194]. The uppercase English letter denotes the electron shell (K, L, M, ...) that the ejected electron originated from. The Greek letter illustrates the general order of X-ray intensities for photons originating from electron relaxation to that shell with $\alpha > \beta > \gamma$. The number subscript indicates the relative intensities of X-rays with the same letter combinations. For example, the $K\alpha_1$ radiation will be the highest intensity X-ray radiation originating from electron relaxation to the K shell (1s orbital) of a given atom.

The specific transitions that can take place giving characteristic X-rays are determined by a set of quantum mechanical selection rules. These rules are centered on the specific combinations of quantum numbers (n, l, m and s) for the initial and final states of the relaxing electron. The rules are as follows:

- $\Delta n \geq 1$:
  n is the main quantum number, defining the electron shell. This rule states that a transition can not happen between two electron states in the same shell.

- $\Delta l = \pm 1$
  l is the angular momentum quantum number, defining the number of electron orbitals in an electron shell, taking values from 0 to n-1. For example, this means that a de-excitation will not take place from 1 2s orbital to a 1s orbital, because they both have the same angular momentum number $l = 0$.

- $\Delta J = \pm 1$, or 0
  J is the sum of $l + s$, where $s = \pm \frac{1}{2}$ is the spin quantum number for electrons. As the X-ray photons have spin numbers of ± 1, it then follows that if spin is to be preserved in the process, the change in total momentum of the relaxing electron must also be ± 1, or 0.

There are a few things to be aware of when performing EDS on a sample. One is that the interaction volume of the beam can be substantially larger than the beam cross-section itself. This is especially important when dealing with bulk samples in a SEM. This means that when measuring the composition of a grain, one should make sure that the grain is larger than the interaction volume (usually on the order of 1-3 µm in diameter) in the SEM. This is generally not a problem in a TEM, since the sample is very thin, which reduces the size of the interaction volume considerably.

One other thing to be considered is the relative fluorescence yields of different elements. For lighter elements, the amount of electronic relaxation leading to an emitted X-ray photon is reduced in favor of emission of Auger electrons. For this reason, EDS is usually not considered suitable for detection of elements lighter than carbon.

3.5.4   X-ray Diffraction (XRD)

Diffraction can be performed with many different types of waves, but X-ray diffraction is one of the most widely used methods for materials characterization. The method is based on the principle of diffraction of x-ray waves in the periodic lattices of crystal structures, as described by the Bragg equation (2.5). There are different experimental set-ups used for this method, but all of them are based around an X-ray source that sends X-rays onto a sample in a range of angles, and a detector which measures the intensity of the diffracted beam for each of the sampled angles, creating an Intensity (counts) versus angle (2θ) graph called a diffractogram. The reason why the diffraction angle is described by 2θ instead of θ is a result of the specific geometry of the X-ray source, sample and detector in the instrument.

The X-rays used for the diffraction experiments are characteristic X-rays produced in so-called X-ray tubes under vacuum by sending high-speed electrons accelerated by a strong electric field onto a metal target (often Cu). The process creating the X-rays is the same as described in the EDS section (3.5.3). In addition to the characteristic X-rays, there is also created a continuous spectrum of X-rays from the rapid deceleration of the incident electrons due to the electric fields experienced by the electrons when they enter the metal target. This continuous spectrum of X-ray radiation is called bremsstrahlung ("breaking radiation"). In order to filter out this continuous spectrum of wavelengths and obtain only the characteristic X-rays wanted for the diffraction experiments, a monochromating X-ray filter is used which absorbs all the undesired wavelengths and lets only the specific wavelengths of the caracteristic radiation through [33, p. 63]. Figure 3.6 shows a schematic of an X-ray tube used for XRD.
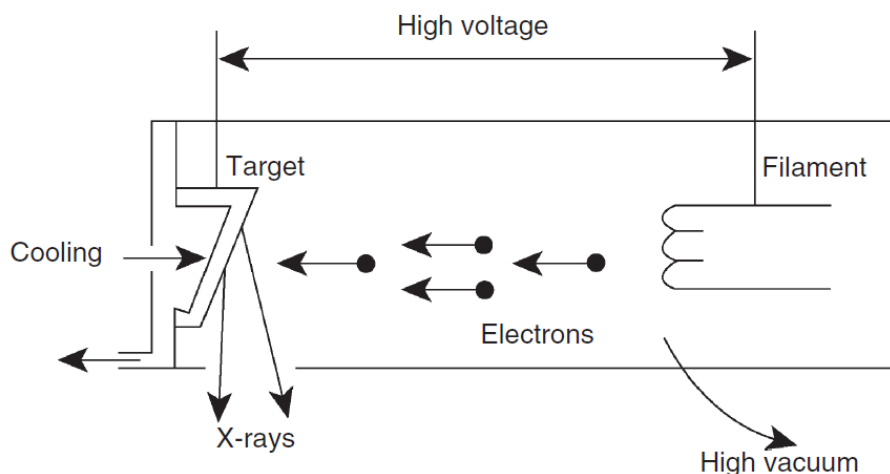
Figure 3.6: Schematic of an X-ray tube showing high speed electrons accelerated by a high voltage hitting a metal target and generating X-ray radiation. Figure copied from [33]

The rest of the XRD instrumentation is dependent on the specific types of samples they are used for, but the majority of commercially available diffractometers use the Bragg-Brentano arrangement. Here, the position and angle of the incident X-ray is fixed, but the sample stage is tilted in order to change the incident angle of the beam relative to the sample.

X-ray diffraction (XRD) is often performed on powdered samples, containing small grains in many different orientations in order for all possible crystal planes to be detected by the X-ray beam. The beam illuminates the sample in a range of angles, and the diffracted intensity is recorded for each angular increment. Unlike SAED performed in a TEM, XRD is performed on the whole sample at once. This means that all phases present in the sample volume will contribute to the recorded diffractogram. For multi-phase samples with unknown phases, this can make structure identification a bit more difficult. Where XRD performs much better than SAED is in the accurate determination of planar distances. By mixing in a standard sample, often finely powdered silicon, the signal can be very accurately calibrated.

Relative intensities of specific reflexes are also quite straightforward to interpret from XRD as these depend on atomic X-ray scattering factors and atomic plane multiplicities, giving extra information on sample composition and structure. This interpretation is much more difficult in SAED since the relative intensities of the different reflexes change dynamically depending very much on sample thickness, which can often be difficult to measure accurately.

If the X-rays that are used for XRD are energetic enough, their energy can sometimes be absorbed by electrons in the sample, which can then lead to radiative relaxation. This radiation is released in all directions, which can cause so-called fluorescence noise in the recorded spectra. Fluorescence noise can cause a problem when using high energy X-ray radiation on samples containing elements with high fluorescence yields and electrons with work functions smaller than the energy of the phonons. In the case of Cu $K\alpha$ radiation, this can cause problems in samples containing, for example, Fe and Ni. This problem can be avoided by using a fluorescence suppressing filter, which will also decrease the overall intensity of the desired signal, or by increasing the runtime of the diffraction experiment to increase the signal/noise ratio.

Chapter 4

Results

4.1 M₂Si-1.0

SEM imaging, as well as EDS mapping performed on the as-cast samples of the M₂Si-1.0 composition revealed three distinct phases, as shown in Figure 4.1. The main phase (marked 1 in the image) can be seen as large, grey dendrites in the image. The phase marked '2' in the image can be seen as bright, thin areas that appear along the grain boundaries between the phase 1 grains. The third phase is visible as smaller, darker grey grains inside some of the areas of phase 2. EDS mapping showed that most of the Cu in the specimen had segregated into the interdendritic regions (phase 2), and did not mix well with the other elements.

(a)   (b)
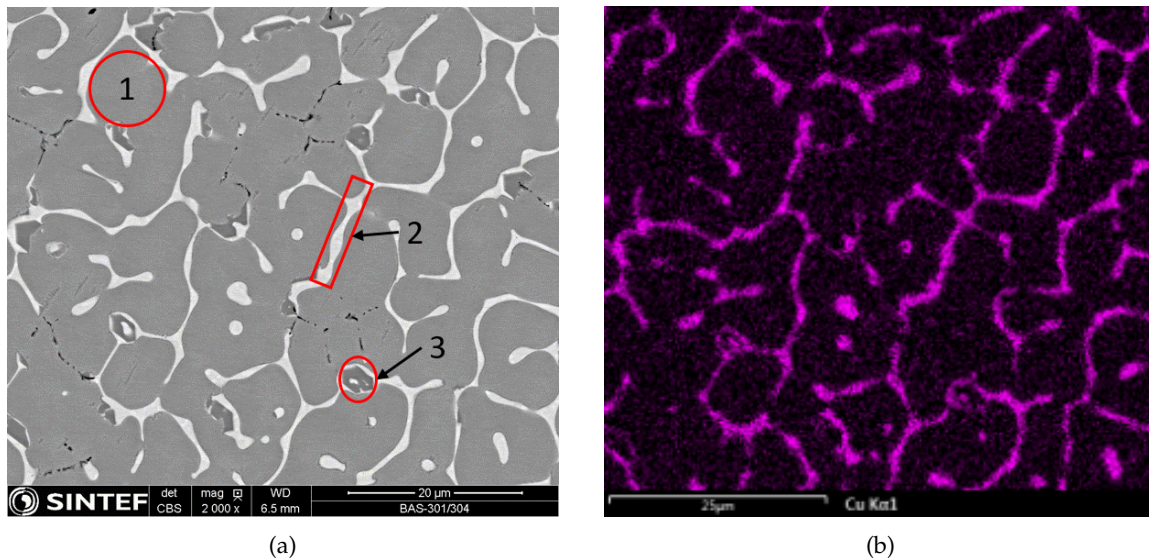
Figure 4.1: **a)** BSE SEM image of as-cast bulk M₂Si sample showing three distinct phases, marked 1, 2, and 3. **b)** EDS map showing the distribution of Cu in the sample. The map reveals that most of the copper in the sample is segregated into the interdendritic regions, with a very low Cu concentration in the other phases.

Figure 4.2 shows the distribution of the phases after annealing at 800 °C for 8 hours, as well as the distribution of copper and chromium in the sample. The BSE SEM images revealed some apparent growth of the phase 2 and 3 grains. EDS mapping confirmed that the bright phase 2 grains were still very rich in Cu relative to the rest of the sample, and also that the phase 3 grains were enriched in Cr.
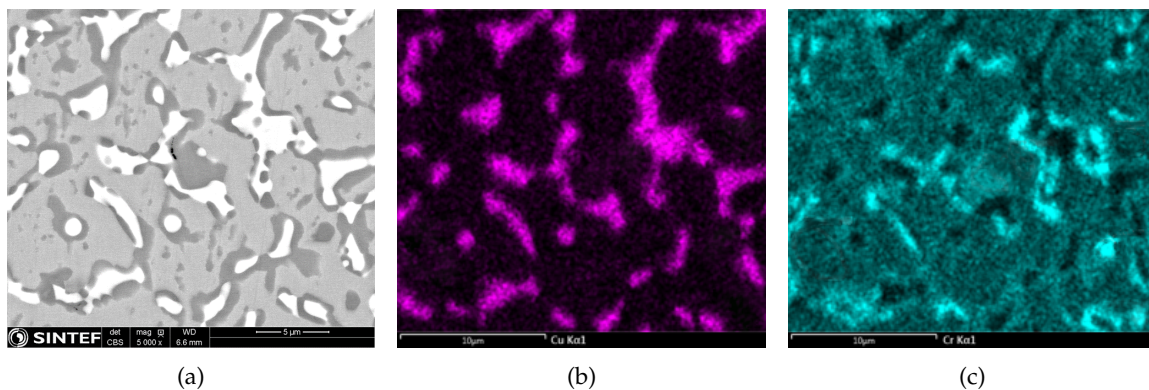

(a)   (b)   (c)

Figure 4.2: **a)** BSE SEM image of the annealed bulk M₂Si sample showing the three phases observed in the as-cast sample. **b)** EDS map showing the distribution of Cu. **c)** EDS map showing the distribution of Cr.

SEM EDS spectra from the matrix phase of the bulk sample showed an average composition of $Si_{32}Cr_{14}Co_{18}Fe_{18}Ni_{18}$. In an attempt at producing a single-phase sample, a new sample was made (M_2Si-1.1) with the nominal composition of the matrix phase from sample M_2Si-1.0b.

4.2 M_2Si-1.1

Initial SEM observations of as-cast bulk samples of M_2Si-1.1 showed that the goal of producing a single-phase sample was not achieved. In an attempt at stabilizing the matrix phase from the previous sample that had been the goal of this casting, the sample was subsequently annealed, this time at 900 °C for 40 hours. Figure 4.3 shows two BSE SEM images taken of the annealed sample. The images show that segregation of the matrix phase had taken place, resulting in a Widmanstätten type microstructure [37] visible throughout the matrix of the sample. several approximate 120° angles could also be observed along the edges of the phase 1 grains. This is particularly visible in the marked phase 1 grain in Figure 4.1b).
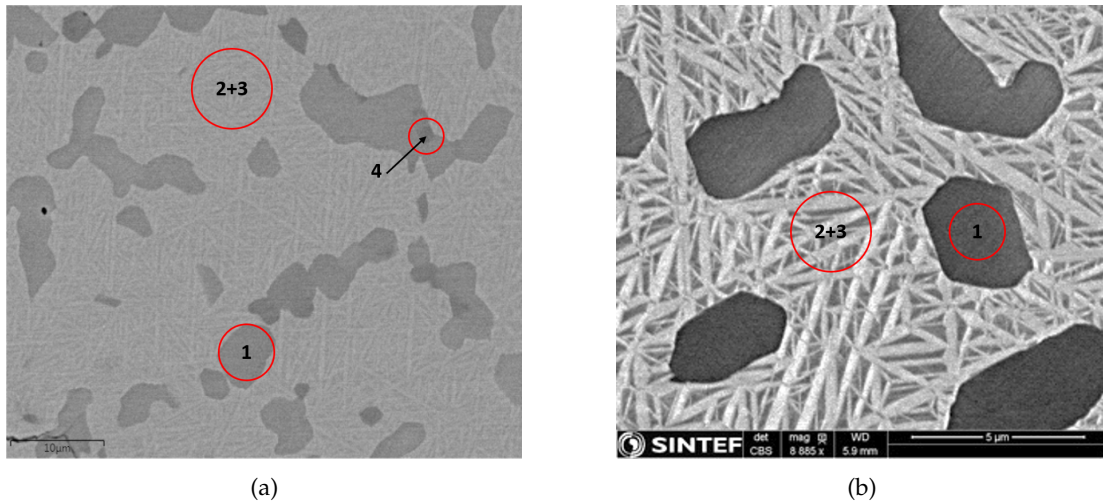

(a)   (b)

Figure 4.3: **a)** BSE SEM image of M_2Si-1.1b. Four distinct phases can be observed. **b)** Higher magnification BSE SEM image of the same sample where the main three phases can be observed. approximate 120° angles can be observed in several places along the edges of the phase 1 grains. Both images show large dark grains (phase 1) surrounded by a matrix consisting of two phases creating a Widmanstätten structure (phases 2 and 3).

There were four distinct phases visible during SEM observation. However, EDS measurements on the minority phase revealed a non-HEA composition, and since there was significantly more of the three main phases present in the sample than of the darker minority phase, this phase has been disregarded in further studies. EDS results from the fourth phase can be seen in chapter 8.

4.2.1 Identification of structures with XRD

Initial XRD measurements were performed in the range $10 - 90°$. Because of the CuK_α X-ray source, fluorescence noise was a problem in the first round of measurements. In the next round of measurements, this problem was alleviated by extending the run time from 90 mins to 14 hrs. Figure 4.4 shows a part of the recorded diffractogram, selected to display the most prominent peaks. The full diffractogram can be viewed in chapter 8.

Recorded XRD peaks from the sample were wide when compared to the Si standard peaks, contributing to some challenges in identifying peaks. However, convincing matches were found for the Fe$_5$Si$_3$ and Ni$_2$Si structures, as shown in Figure 4.4. It can also be observed that the peaks corresponding to the Ni$_2$Si structure were somewhat wider relative to the peaks corresponding to the Fe$_5$Si$_3$ structure.
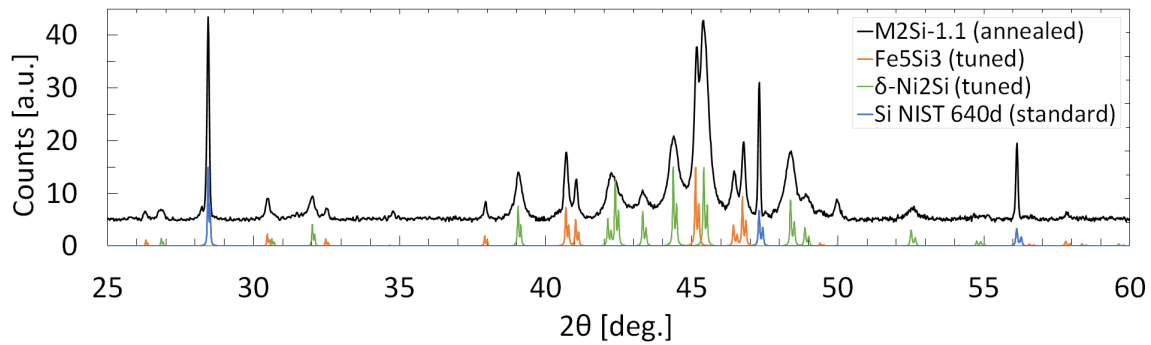

Figure 4.4: XRD of M$_2$Si-1.1 sample, showing a comparison of the experimental diffractogram from $2\theta = 25 - 90°$ with simulated diffraction peaks for the Fe$_5$Si$_3$ and Ni$_2$Si structures. This range was chosen to show the most prominent peaks. The full diffractogram can be seen in chapter 8.

After initial tuning of cell parameters, further refining yielded the lattice values that were used for further investigation. A summary of the two structures can be seen in table 4.1

Table 4.1: Summary of tuned structure matches from XRD fingerprinting.

Structure type	Crystal system	Space group symbol	(Tuned) Lattice constants
Fe$_5$Si$_3$	Hexagonal	P6$_3$/mcm (193)	$a = 6.770$ Å $c = 4.743$ Å
Ni$_2$Si	Orthorombic	Pbnm (62)	$a = 7.065$ Å $b = 5.173$ Å $c = 3.759$ Å

4.2.2 Determining Phase Compositions and Distribution

With two candidate structures proposed for the three main phases in the sample, TEM and STEM was used to confirm the XRD results and further identify which structures belonged to which phases, as well as for investigation of the sample microstructure and inter-phase orientation relationships.

Figure 4.5 shows a DF STEM image of an area of the bulk TEM sample of M_2Si-1.1. The image showed a complex microstructure, with phase 1 visible as the wide grains with uneven edges. Phase 2 can be seen as the brighter, wider lamellas, and phase 3 as the darker, narrower lamellas. Closely set lines could also be seen across some of the phase 3 grains. A significant amount of strain in the sample could be observed, as can be seen in the lower right quadrant of the image.
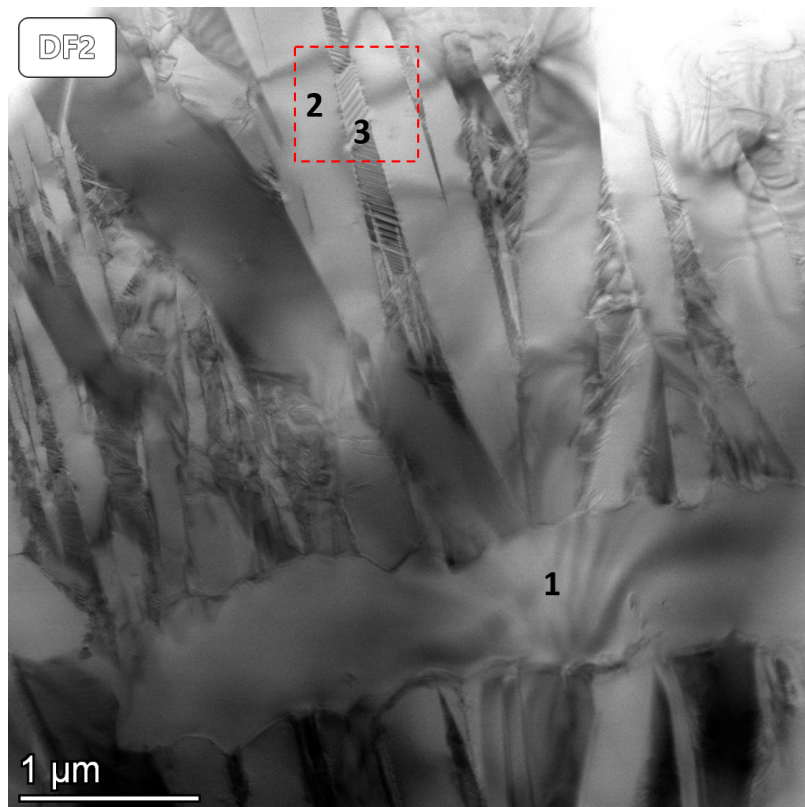
Figure 4.5: STEM DF image of the $M_2Si1.1b$ sample showing an area with all three main phases visible and a complex microstructure. Dense, straight lines are visible within some of the grains of phase 3. The image reveals strain that was also visible in several other areas of the sample. The area marked by the red box shows where some further investigations into phase 2 and 3 were performed. These are presented in Figure 4.7.

Figure 4.6 shows a HAADF image with a corresponding EDS map of the chromium and nickel distribution in an area containing all three main phases. This revealed that phase 1 appeared to be richer in Cr and significantly poorer in Ni than the surrounding matrix. An integrated EDS spectrum from area 1 in Figure 4.6 indicated an approximate composition of $Si_{37}Cr_{22}Fe_{19}Co_{14}Ni_7$. A significant amount of overlap between the phase 2 and 3 grains in this area made extracting quantitative information on these phases challenging.
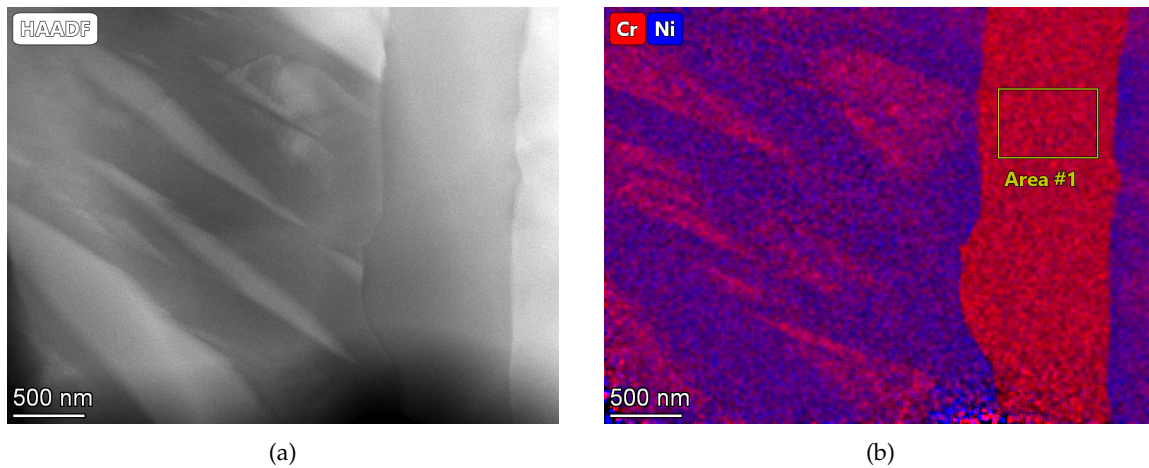
(a)

(b)

Figure 4.6: **a)** HAADF STEM image showing a large grain of phase 1 to the right with uneven edges, and grains of phase 2 and 3 shaped like thinner lines on the left. **b)** EDS maps of Cr and Ni distribution in the different phases. The large uneven grain on the right (phase 1) was richer in Cr and poorer in Ni than both of the lamellar phases on the left. EDS spectrum for Area1 can be seen in chapter 8

Closer investigations of phases 2 and 3 showed that the wider lamellas (phase 2) were richer in nickel and the narrower lamellas (phase 3) were richer in chromium, as can be seen in Figure 4.7. The DF STEM image shows some semi-periodic variation within the phase 3 grains, which is not visible in the corresponding EDS map. The average width of these is found to be around 30-35 nm. These variations also seem to switch between two sets of orientations, indicating twinning in the phase 3 grains, although no diffraction patterns were obtained in areas containing both orientations of the lines.

An integrated EDS line scan was also performed across the two phases in the area marked in Figure 4.7b), showing an approximate composition of $Si_{32}Cr_{12}Fe_{17}Co_{19}Ni_{20}$ for phase 2 and $Si_{32}Cr_{18}Fe_{17}Co_{16}Ni_{17}$ for phase 3. A graphical representation of the measured values from the line scan can be seen in Figure 4.8.

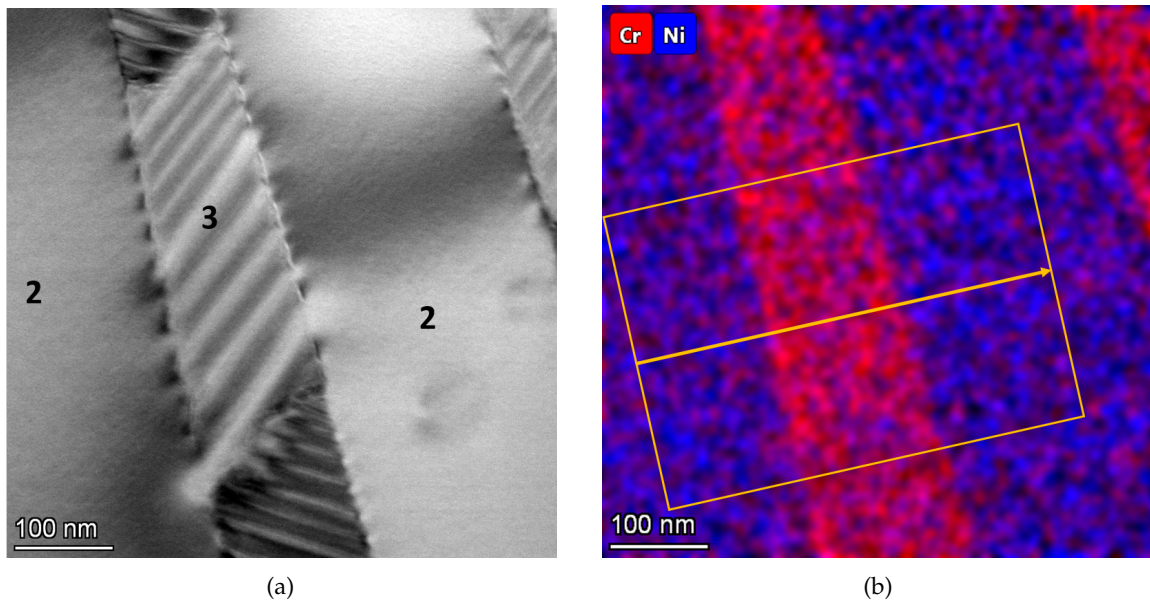<div align="center">(a)   (b)</div>

Figure 4.7: **a)** STEM DF image showing the two lamellar phases, marked 2 and 3 in the image. One can also clearly see defects that look like dislocations along the phase 2/3 interface. The phase 3 grains appear to contain some semi-periodic defects with an average width of around 30- 35 nm. **b)** EDS map showing the Cr and Ni distribution between the two lamellar phases, as well as the area for an integrated line scan across both phases. The results of the line scan can be seen in Figure 4.8.
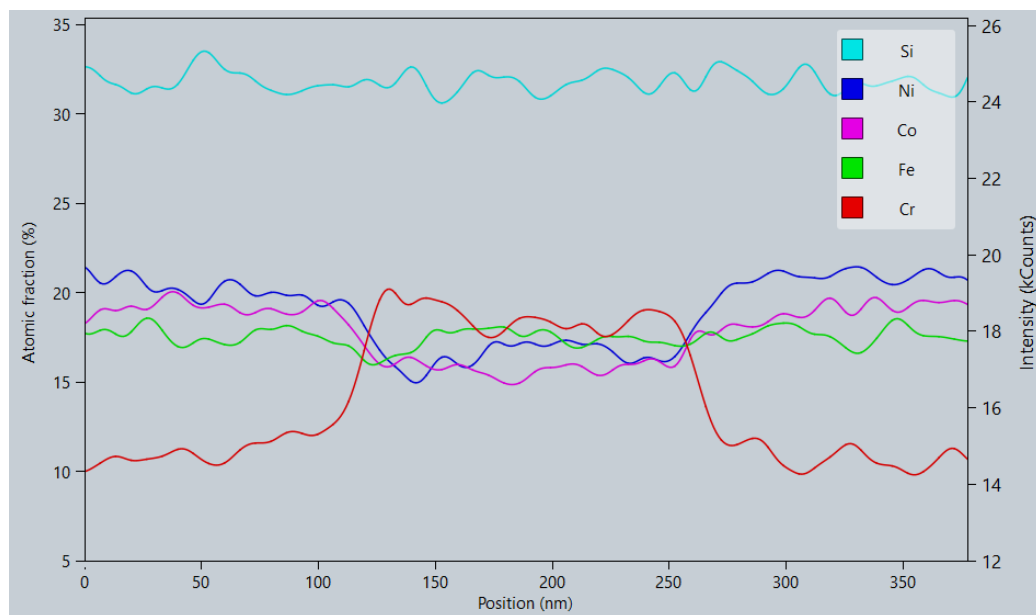
Figure 4.8: EDS line scan from the area marked in Figure 4.7. The scan confirms the observations from the Cr and Ni maps in Figure 4.7, showing a significant increase in chromium content in phase 3 relative to phase 2. Corresponding decreases in nickel and cobalt are also visible in the same area.

A summary of the EDS results for the three main phases can be seen in table 4.2. This shows that phase 2 and 3 fall comfortably inside the compositional requirement for HEAs outlined in section 1.2.2, while phase 1 is a little too rich in silicon to fulfill the compositional requirement of at least five major elements present in between $5 - 35$ at%.

Table 4.2: Phase composition summary from EDS

Phase	Si [at%]	Cr [at%]	Fe [at%]	Co [at%]	Ni[at%]
1	37	22	19	14	7
2	32	12	17	19	20
3	32	18	17	16	17

4.2.3 Matching Structures With Phases

SAED patterns acquired from phase 1 are shown in figures 4.9 and 4.10. These could be indexed in agreement with the [210] and [211] zone axes (ZAs) of the Fe_5Si_3 structure. There are some reflexes in the experimental patterns that are not accounted for in the simulated ones, marked with circles in the figures. However, it is probable that these reflexes are the result of dynamic scattering. Both the zero-order and first order Laue zone (ZOLZ and FOLZ) patterns showed good agreement between experiment and simulation, which lead to the conclusion that phase 1 has the Fe_5Si_3 structure.
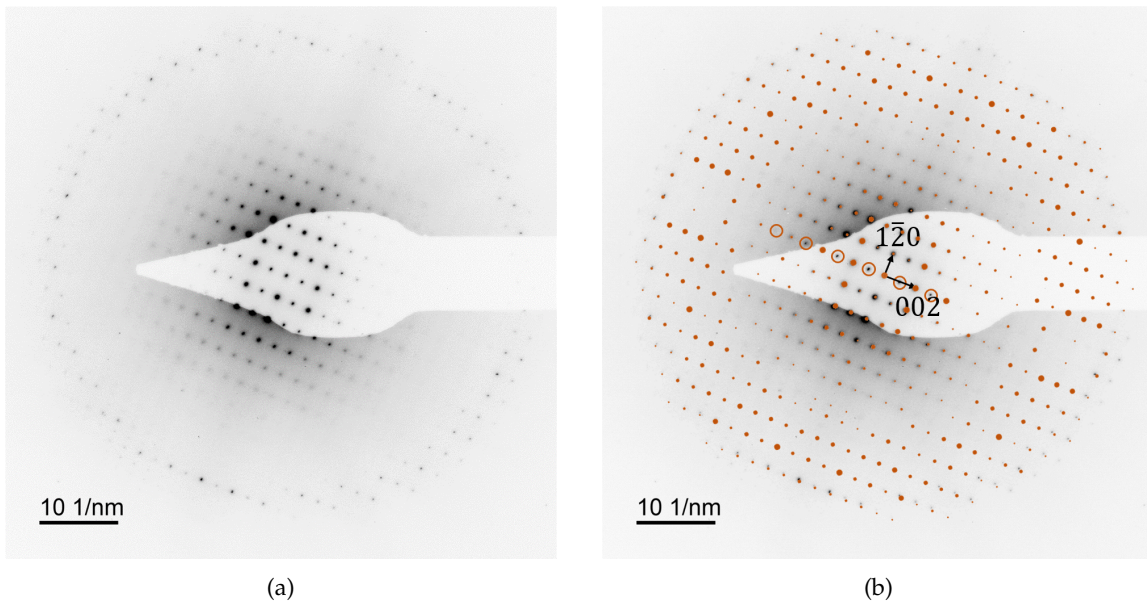

Figure 4.9: **a)** Experimentally obtained SAED from phase 1, showing both the ZOLZ and FOLZ patterns. **b)** The simulated diffraction pattern of the Fe_5Si_3 [210] zone axis, superimposed onto the experimentally obtained pattern. The patterns show very good agreement in both the zero- and first-order Laue zones. Reflexes assumed to be results of dynamic scattering are marked with circles.
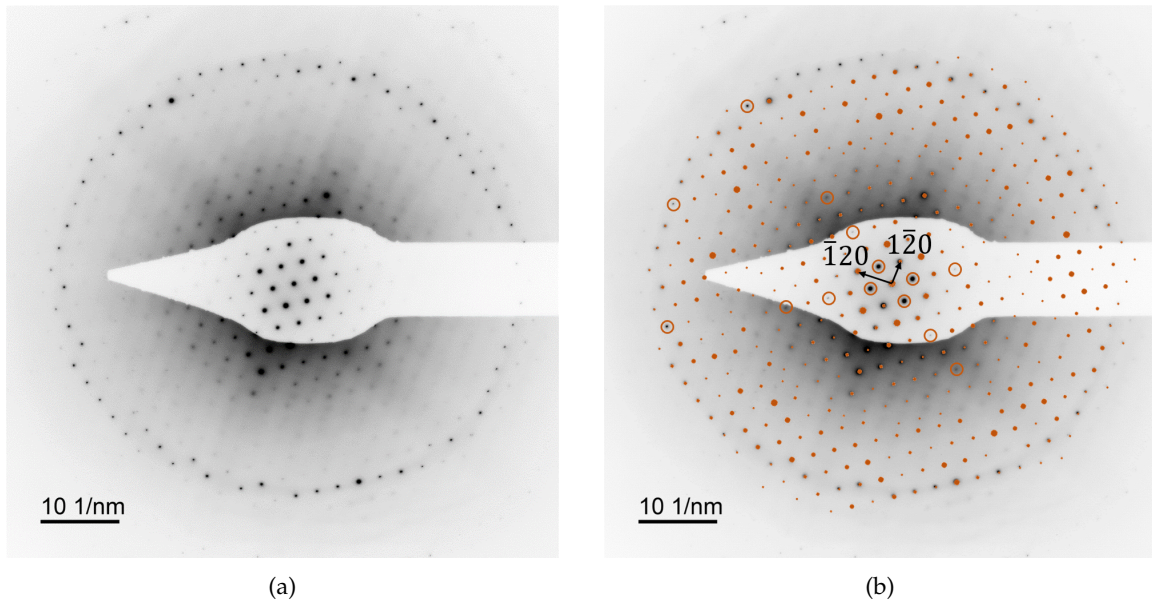
(a)

(b)

Figure 4.10: **a)** Experimentally obtained SAED from phase 1 in a different tilt relative to Figure 4.9, showing both the ZOLZ and FOLZ patterns. **b)** The simulated diffraction pattern of the Fe_5Si_3 [211] zone axis, superimposed onto the experimentally obtained pattern. The patterns show very good agreement in both the zero- and first-order Laue zones. Reflexes assumed to be results of dynamic scattering are marked with circles.

The first SAED pattern from phase 2, as seen in Figure 4.11 was obtained in the same area as the one imaged in Figure 4.7. This showed a good match for the Ni_2Si [111] ZA, except for some reflexes that should be extinct if only kinetically scattered electrons contributed to the pattern.
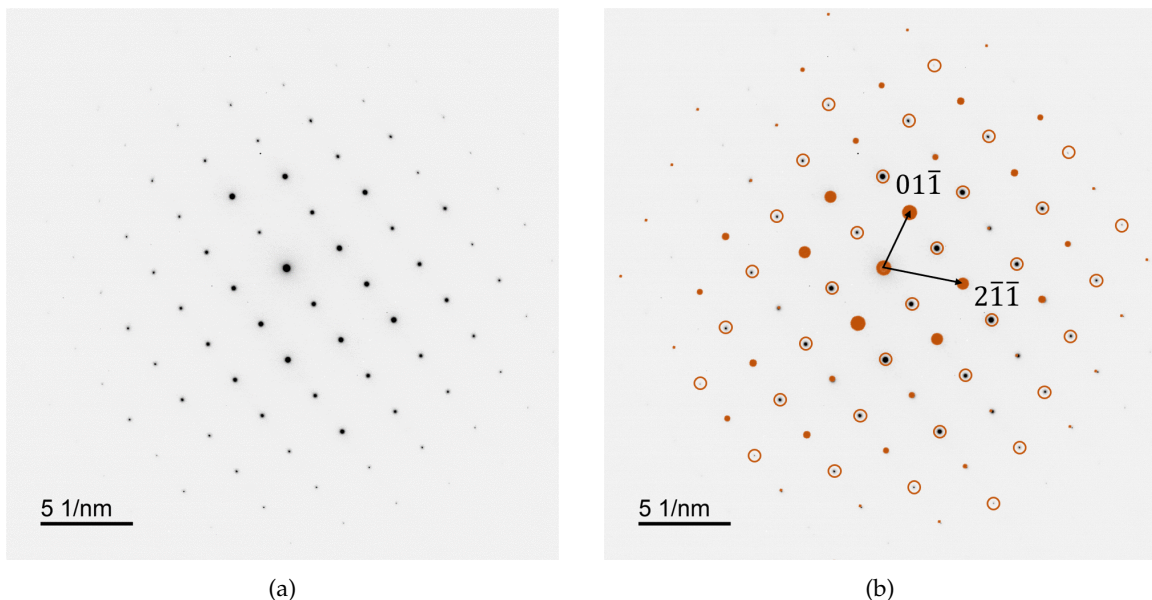

(a)

(b)

Figure 4.11: **a)** Experimentally obtained SAED pattern from phase 2. **b)** The simulated diffraction pattern of the Ni_2Si [111] ZA, superimposed on the experimental SAED pattern, showing a good agreement between experiment and simulation. Reflexes that are assumed to stem from dynamic scattering are marked with circles.

Another SAED pattern obtained from phase 2 in the same area could be indexed in agreement with the [001] ZA of Ni$_2$Si, with the exception of some discrepancy between experiment and simulation with respect to the **b**/**c** ratio, as seen in Figure 4.12.

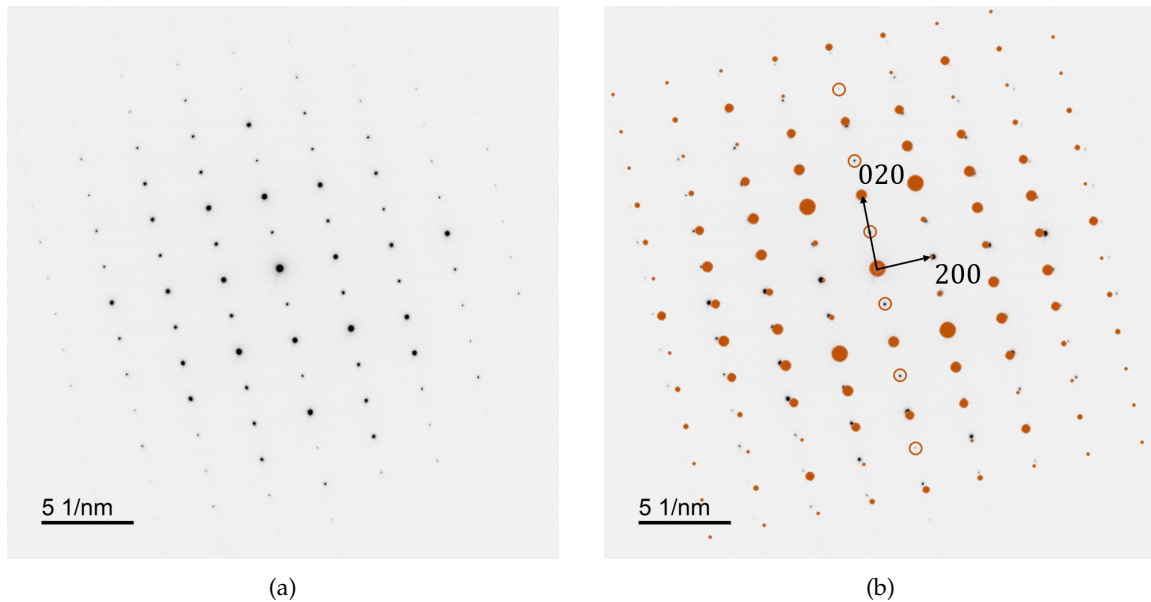(a)   (b)

Figure 4.12: **a)** Experimentally obtained SAED pattern from phase 2. **b)** The same image, with a simulated SAED pattern from the Ni$_2$Si [001] ZA superimposed.

In order to increase confidence in the phase identification, a high resolution HAADF image of phase 2 in the same orientation as the one seen in Figure 4.12 was recorded. The image showed a convincing match to the Ni$_2$Si structure in the [001] orientation, as can be seen in Figure 4.13.

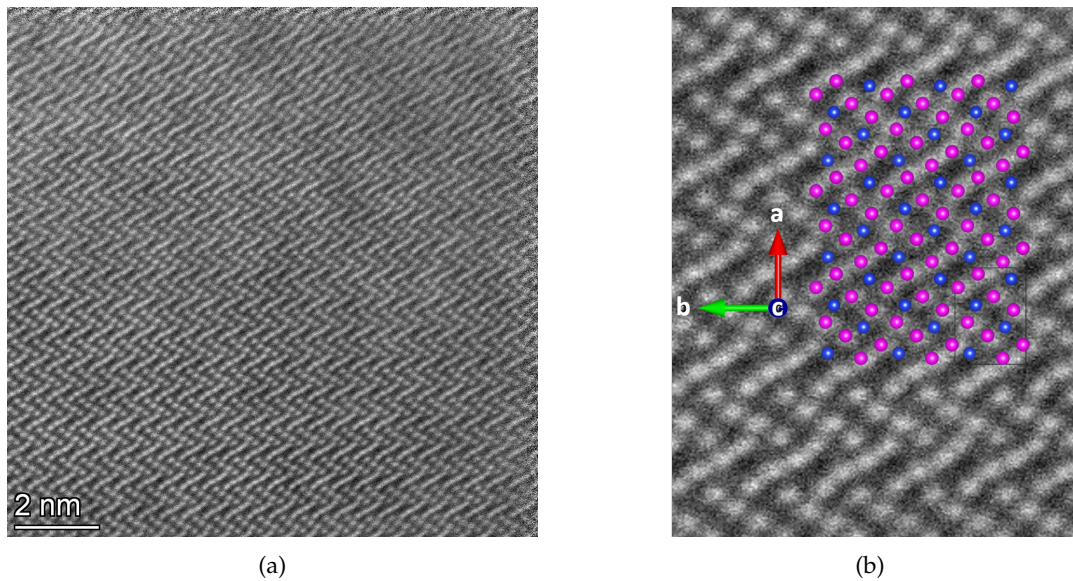(a)   (b)

Figure 4.13: **a)** High resolution HAADF image from phase 2 in the same orientation as the SAED pattern in Figure 4.12. **b)** Enlarged cutout of a), with a simulated Ni_2Si 3x3x3 supercell in the [001] orientation superimposed. The Ni (or in the case of phase 2, mixed metal) atoms are pink and the Si atoms, blue. The image shows a very good agreement between experiment and simulation. Heavier elements appear brighter HAADF images, corresponding well with the atomic masses of silicon relative to the different alloying metals.

SAED from phase 3 were obtained in the same area as the one shown in Figure 4.7 and at the same tilts as the SAED patterns shown for phase 2. As can be seen from the image in Figure 4.14, the smallest SAED aperture available in the microscope was too large to select only phase 3 to contribute to the recorded SAED pattern. Consequently, the obtained diffraction patterns shown in Figures (4.11 and 4.12) have contributions from both phases 2 and 3.
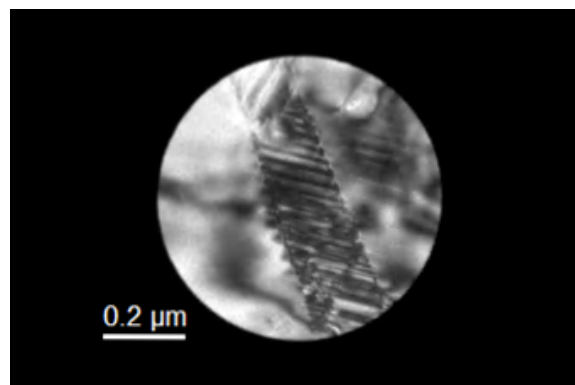

Figure 4.14: Image showing the area selected by the smallest SAED aperture (500 nm diameter) available in the microscope. Both phase 2 and 3 are clearly visible within the aperture in the image.

The DP visible in Figure 4.15 was taken in the same orientation as Figure 4.12. The pattern showed what appeared to be an almost complete overlap of the DPs from the two phases. Consequently, the combined pattern could also be indexed in agreement with the the [001] ZA of Ni_2Si. Although neither the match for the SAED pattern from phase 2 (Figure 4.12) were perfect, the overlapping pattern showed a closer agreement between experiment and simulation.

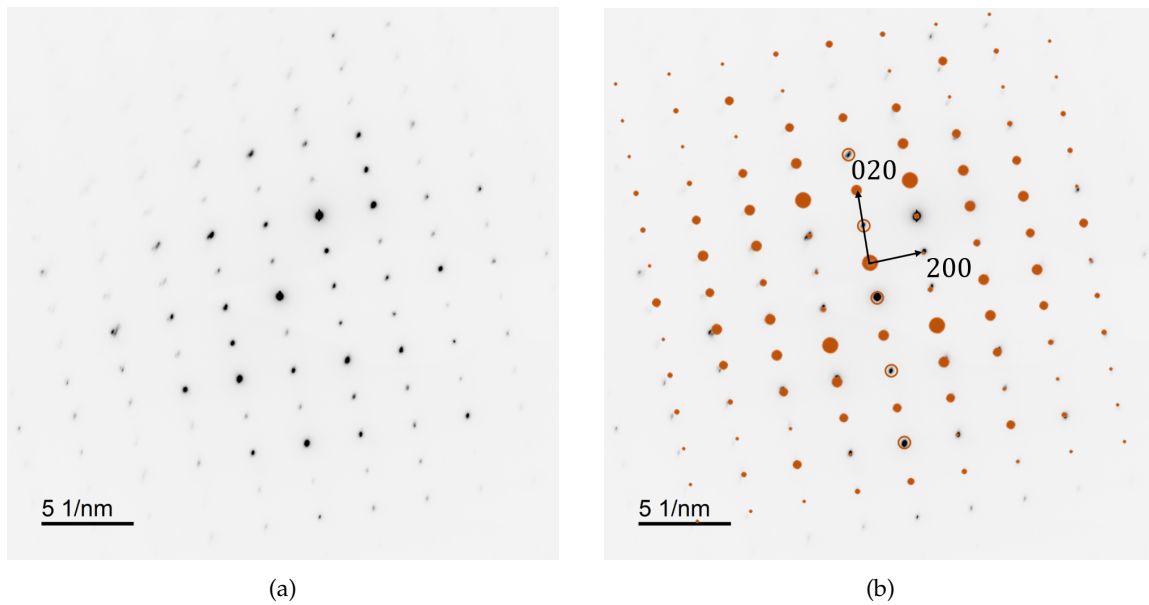(a)   (b)

Figure 4.15: **a)** Experimental SAED obtained from area containing both phase 2 and phase 3, in the same tilt as the pattern shown in Figure 4.12. Certain reflexes in the pattern reveals some strain in the structures. **b)** Experimental pattern with simulated pattern from the Ni_2Si [001] ZA superimposed. The agreement between simulation and experiment was somewhat closer for this pattern than for the one solely originating from phase 2.

The SAED pattern visible in Figure 4.16 was obtained at the same tilt as for the SAED pattern in Figure 4.11. The overlapping patterns appeared to have some reflexes partly or completely overlapping, as well as some stemming exclusively from one of the phases. As the contribution from the phase 2 Ni_2Si [111] ZA was known from the match made in 4.11, this was used as a starting point in identifying the reflexes that had to be accounted for by the DP from phase 3. The remaining reflexes could be indexed with the Ni_2Si [1-11] ZA. The [-111] and [11-1] ZAs were also matches, but the [1-11] was chosen because it had a common crystallographic direction with the pattern from phase 2. This will be addressed in section 4.2.4.

(a)   (b)
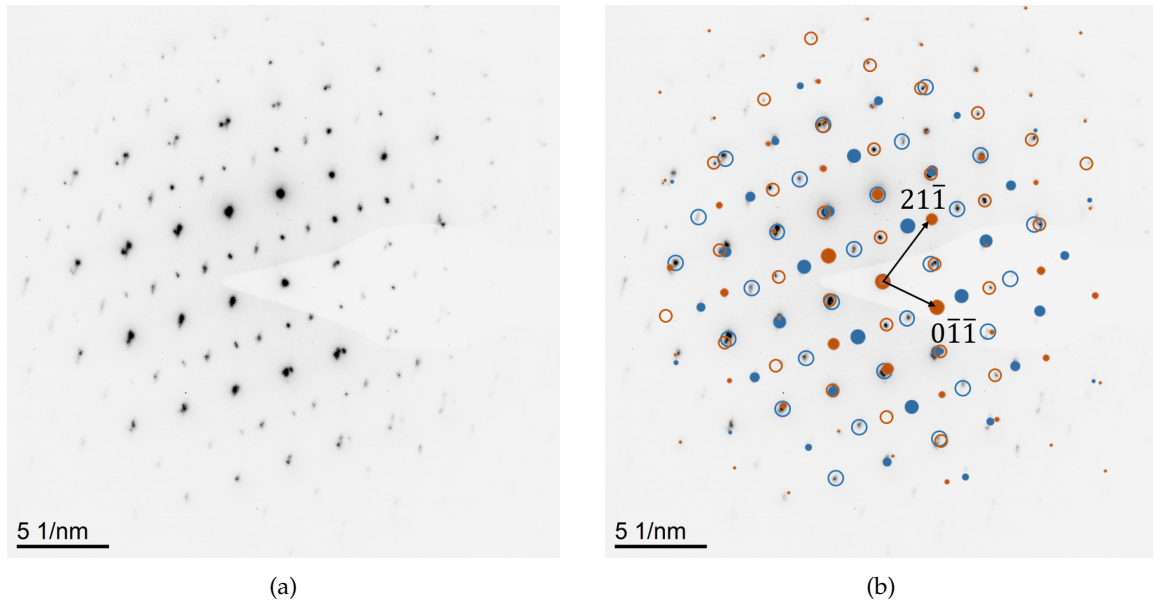
Figure 4.16: **a)** Experimentally obtained SAED pattern from phase 2 and 3, taken in the same area as those shown for phase 2, at the same tilt as the one shown in Figure 4.11. **b)** Experimentally obtained pattern, with an overlap of simulated patterns from the Ni_2Si [111] ZA (blue) originating from phase 2 and the Ni_2Si [1-11] ZA (orange) from phase 3.

A high-resolution STEM image of phase 3 is shown in Figure 4.17. A convincing match to the atomic arrangements observed in the image could be found for the [011] orientation of the Ni_2Si structure. This, together with the obtained electron diffraction lead to the conclusion that both phases 2 and 3 did indeed take the Ni_2Si structure.
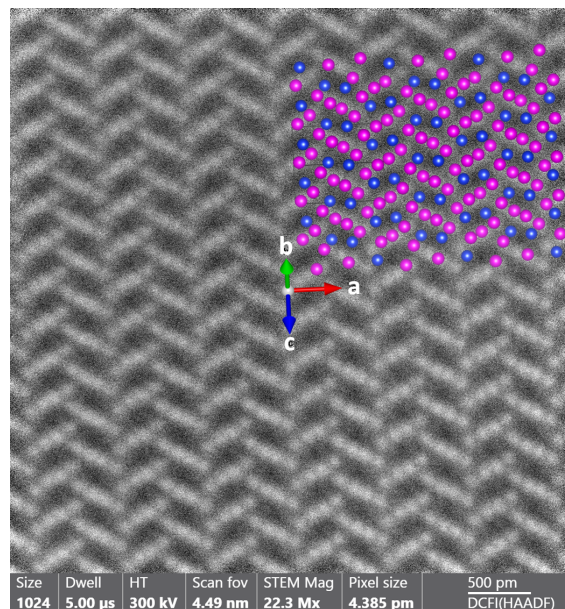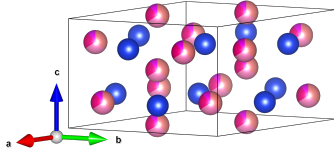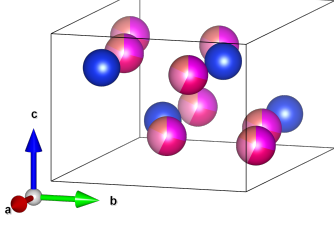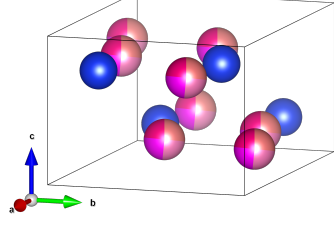

Figure 4.17: HAADF image of phase 3 overlaid with simulated Ni_2Si 3x3x3 supercell in [011] orientation, showing a very good agreement between experiment and simulation.

In summary, all three phases appear to have adopted the structures of known binary transition metal silicides, with the two lamellar matrix phases adopting the same structure types. High resolution HAADF images in combination with compositional M:Si ratio indicate disorder only on the metal sites of the structures. Table 4.3 shows the compositions and structure types of the different phases, as well as a proposed unit cell based on assumed site occupations.

Table 4.3: Summary of structure and composition of M$_2$Si1.1 phases

Phase	Structure Type	Phase Composition (approximate)	Unit Cell
1	Fe$_5$Si$_3$	Si$_{37}$Cr$_{22}$Fe$_{19}$Co$_{14}$Ni$_7$	
2	Ni$_2$Si	Si$_{32}$Cr$_{12}$Fe$_{17}$Co$_{19}$Ni$_{20}$	
3	Ni$_2$Si	SI$_{32}$Cr$_{18}$Fe$_{17}$Co$_{16}$Ni$_{17}$	

4.2.4   Microstructure and orientation relationships

As seen in the SAED pattern in Figure 4.16, there is a common crystallographic direction for the phase 2 and phase 3 grains contributing to the DP. From Figure 4.18, this common direction can be indexed as the [10-1] crystallographic direction. This is also perpendicular to the direction of the interface between the phases, and indicates that the (10-1) crystallographic plane in the Ni_2Si is one of the preferred phase 2/3 interfaces.
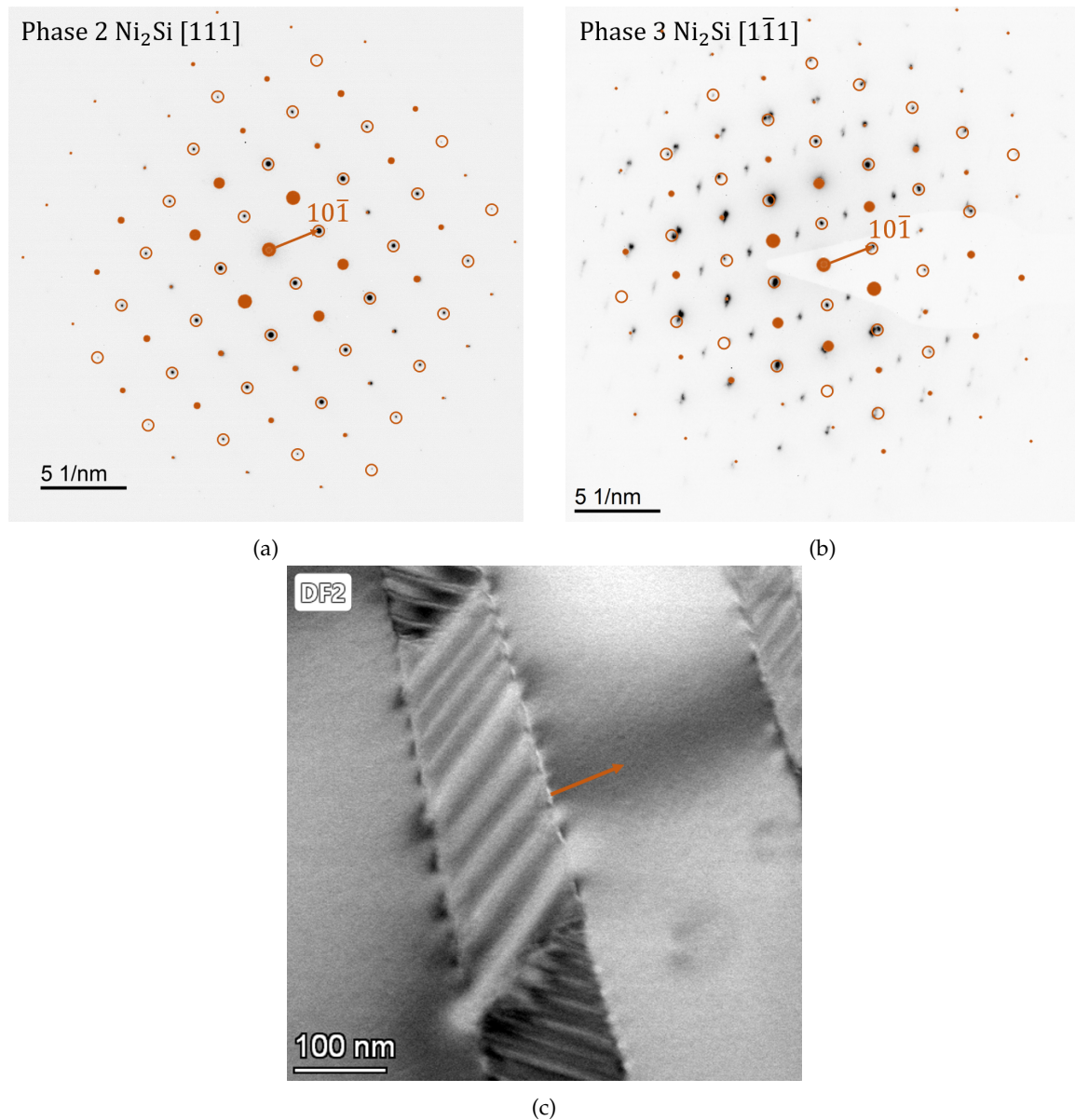

(a)

(b)

(c)

Figure 4.18: **a)** SAED pattern from phase 2 identified as showing the Ni_2Si structure [111] ZA. The [10-1] crystallographic direction is shown in the image. **b)** SAED pattern from both phase 2 and 3 in the same area and tilt with the phase 3 contribution to the pattern identified as coming from the Ni_2Si structure [1-11] ZA. The [10-1] crystallographic direction is shown here to be parallel to the same direction in phase 2. **c)** DF STEM image from the area of the DPs showing that the [10-1] crystallographic direction common for the crystals of the two phases appears to be orthogonal to the interface between the phases.

Figure 4.19 illustrates the orientation of the interface between the two phases. The structure is oriented to look down the common [10-1] direction, and mirrored along the **b** axis, as was indicated by the SAED pattern matches made in Figure 4.16.
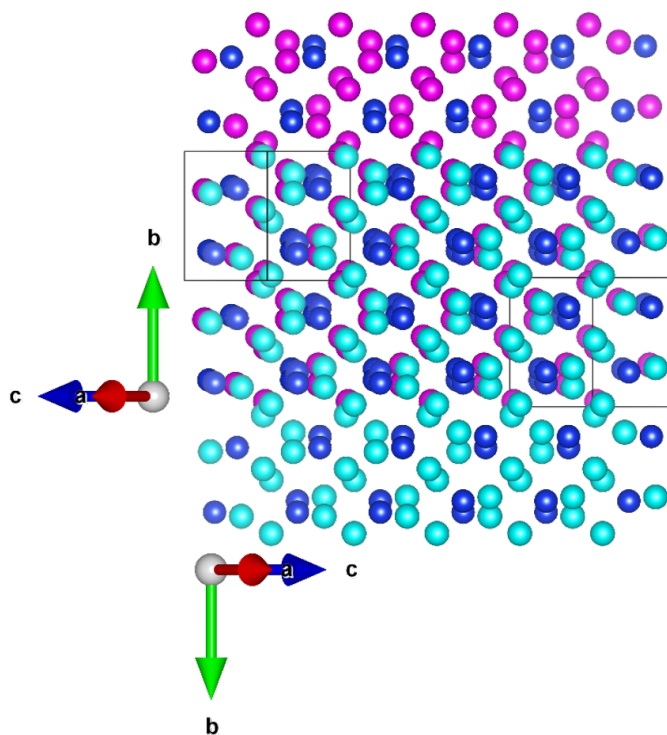

Figure 4.19: Simulation of phase 2, with the metal atoms shown in pink and of phase 3, with the metal atoms shown in turquoise. Both structures are shown along the [10-1] direction, but the phase 3 structure is rotated 180 degrees along the viewing axis so that the two phases are mirrored along the **b** axis. The structures are also slightly shifted relative to each other to allow for better visibility.

Another microstructural feature of interest was the nature of the defects in phase 3, visible in both figures 4.5 and 4.7. In both these figures, the defects can look like periodic variations in crystallographic orientation, known as twinning. However, no sign of twinning was visible from the SAED patterns acquired from the phase. Figure 4.20 shows an orientation of a phase 3 grains, revealing that the variations are planar defects. In the image, the defects can be viewed edge-on, revealing their 2-dimensional nature. In the rest of the image, one can see more of these defects in a slightly different orientation, giving the illusion of a 3-dimensional geometry.
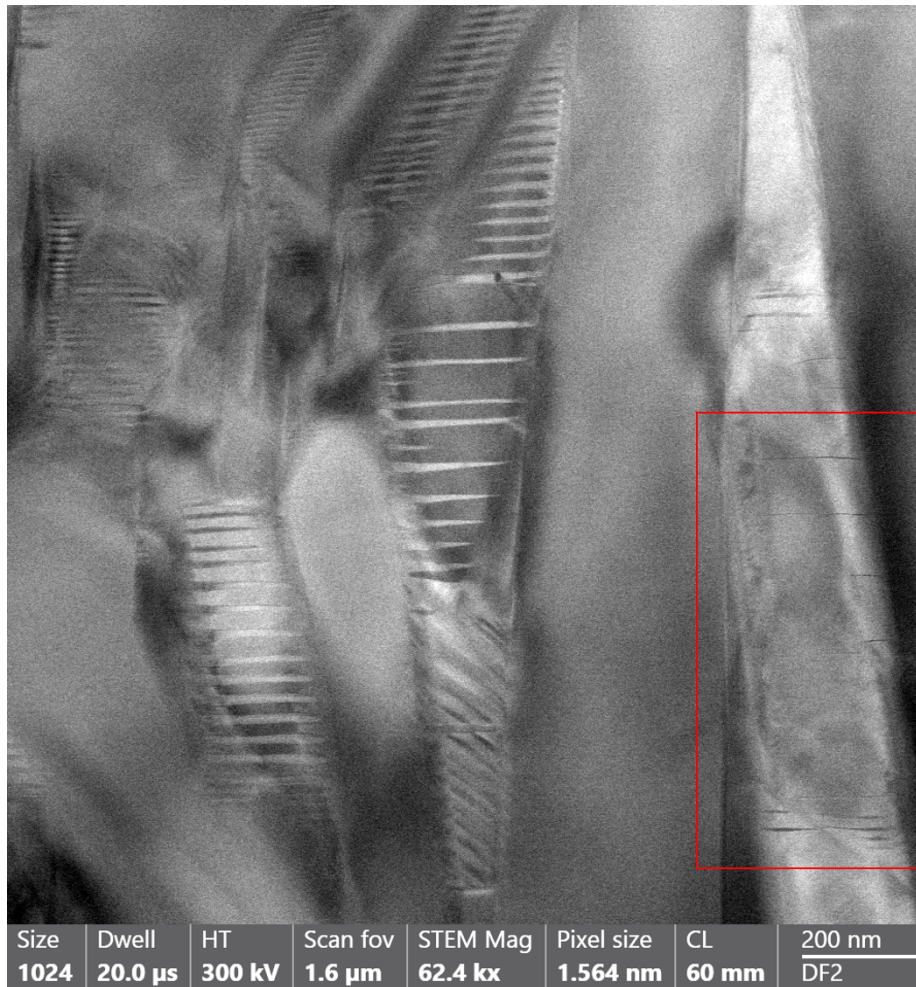
Figure 4.20: DF STEM image showing planar defects (stacking faults) in phase 3. The defects can be seen in slightly different orientations in the different grains, with the tilted orientation of some of them giving the illusion of a 3-dimensional geometry. In the red square on the right, the defects are viewed edge-on, revealing their 2-dimensional nature.

A high-resolution BF STEM image (Figure 4.21) was acquired in the same area as shown in Figure 4.20. The area and orientation was chosen so that the defects were oriented edge-on. The defect itself was not visible in the image, but a darker area could be seen running across the image where the defect was expected to be, indicating strain. A closer look at the image revealed what looked like some sort of wavy pattern going across the image, parallel to the orientation of the defect plane.
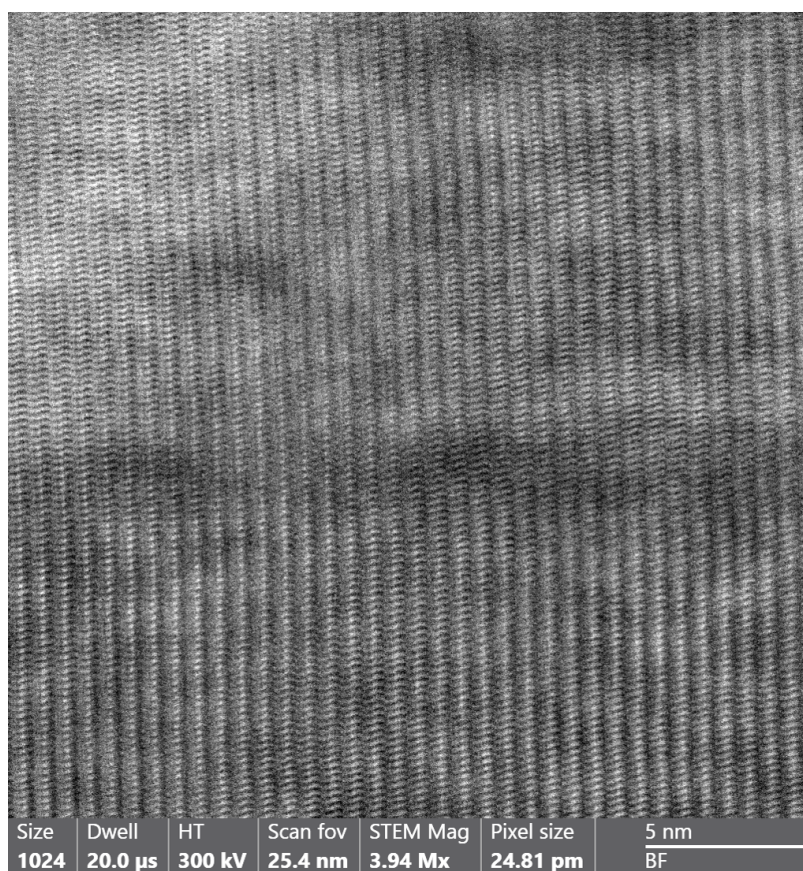
Figure 4.21: High resolution BF STEM image of an area of phase 3 containing a planar defect, oriented edge-on. The defect itself is not visible in the image, but the strain related to it can be seen as a darker area stretching horizontally across the image. The atomic columns appear to make up some sort of wavy pattern, parallel to the orientation of the defect.

To identify the crystallographic orientation of the defect, a fast Fourier transform (FFT) was performed on the image, seen in Figure 4.22. The pattern revealed a high-symmetry ZA, with orthogonal planes. No exact match was found for the ZA, but through combining measurements of distances on the FFT and calculations based on the approximate lattice constants found from the XRD fittings, a probable match was found for the [01-2] ZA of the Ni$_2$Si structure. The measurements and calculations can be viewed in chapter 8.

<table>
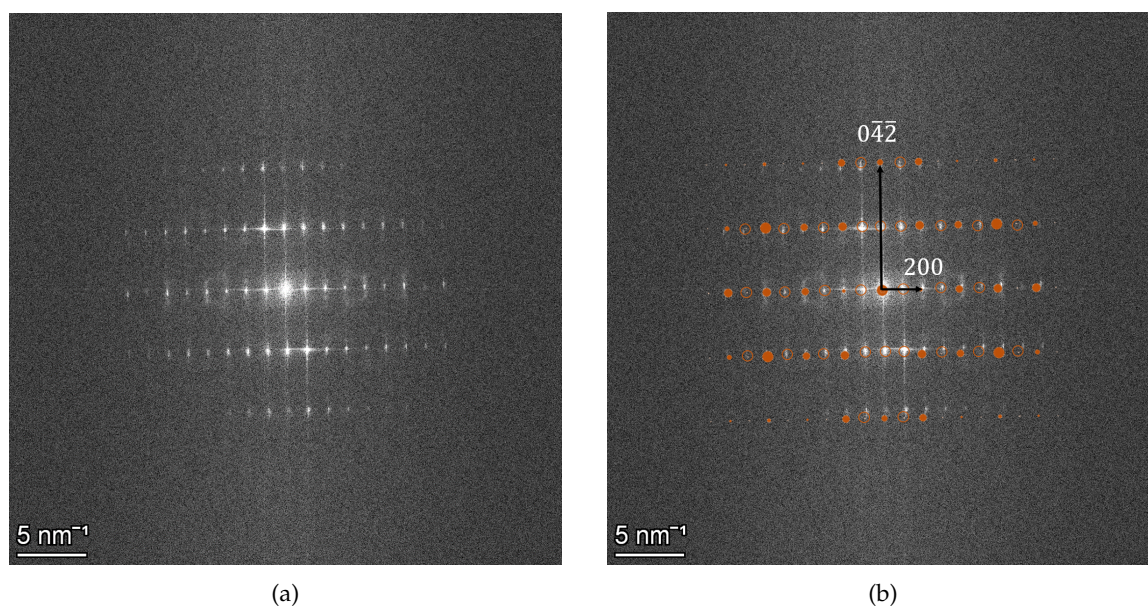<tr><td>(a)</td><td>(b)</td></tr>
</table>

Figure 4.22: **a)** FFT of the image shown in Figure 4.21 showing a ZA with orthogonal sets of reflexes. **b)** FFT overlaid with the simulated DP of the [01-2] zone axis (ZA) of the Ni_2Si structure. There is an acceptable agreement between experiment and simulation, indicating that the stacking faults in phase 3 are parallel to the (012) crystallographic plane.

Figure 4.23 shows the simulated Ni_2Si type structure of phase 3 oriented along the [01-2] crystallographic direction. When looking at the structure, the wavy pattern that could be seen in the high-resolution image in Figure 4.21 could be recognized, strengthening the confidence in the ZA identification. The structure in this orientation displays some relatively densely packed wavy planes of atoms, consisting of both metal and silicon atoms. A fault in the stacking of these layers would not show up in any meaningful way in EDS mapping, as each of the layers consist of a similar amount of both metal and silicon atoms. It seems probable that the defects visible in images of phase 3 are stacking faults in these densely packed layers.
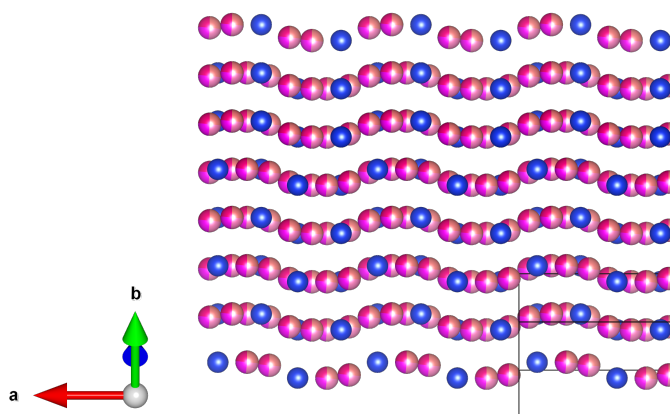

Figure 4.23: Illustration of the proposed structure of phase 3, depicted along the [01-2] crystallographic direction, showing the probable orientation of the phase 3 defect. The observed results are consistent with a fault in the stacking of these dense layers of atoms.

4.3   M$_2$Si-1.2

The purpose of synthesizing this specimen with approximately the same composition as M$_2$Si-1.1 was to gain insight in the as-cast structure of the different phases in the specimen, and also to learn more about any temperature-dependent evolution of the phases and microstructure.

Since the M$_2$Si-1.1 specimen was annealed directly after the initial observation revealed that the goal of producing a single-phase sample was not achieved, no images or data was acquired from the sample in its as-cast state, and it became desirable to try and re-create the system.

4.3.1   M$_2$Si-1.2a

The as-cast M$_2$Si-1.2 specimen was investigated to identify the matrix phase existing prior to the annealing of M$_2$Si-1.1. As can be seen in Figure 4.24, only two phases were visible, with no Widmanstätten microstructure that could be observed. Several ~120° angles could be observed along the edges of the darker grains, indicating a hexagonal crystal structure.
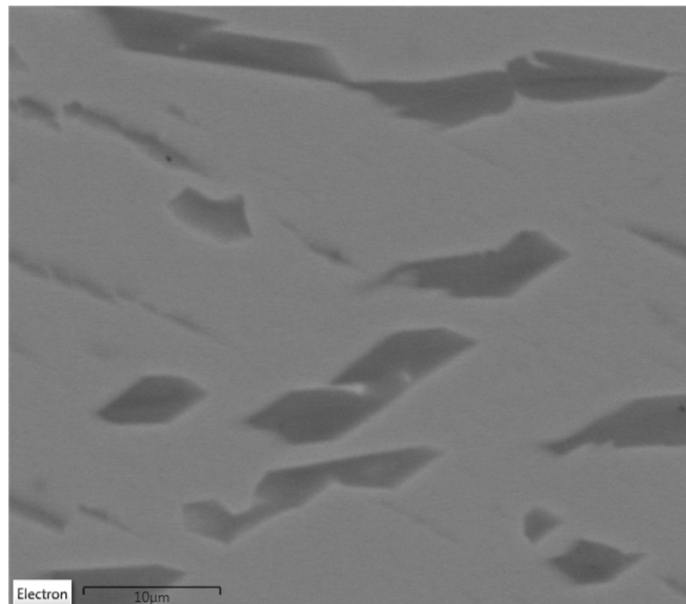
Figure 4.24: BSE SEM image of a sample of the as cast state of the M$_2$Si-1.2 specimen. Two phases are visible in the image, in contrast to the three (actually four) phases in the annealed M$_2$Si-1.1 specimen.

EDS mapping of the silicon, chromium and nickel distribution in the area, as depicted in Figure 4.25 reveal that the relative Si, Ni and Cr contents of the phases follow the same trend as the one demonstrated in the M$_2$Si-1.1 specimen. The maps make it clear that the darker phase in the image in Figure 4.24 is richer in silicon and chromium, and poorer in nickel relative to the matrix phase.
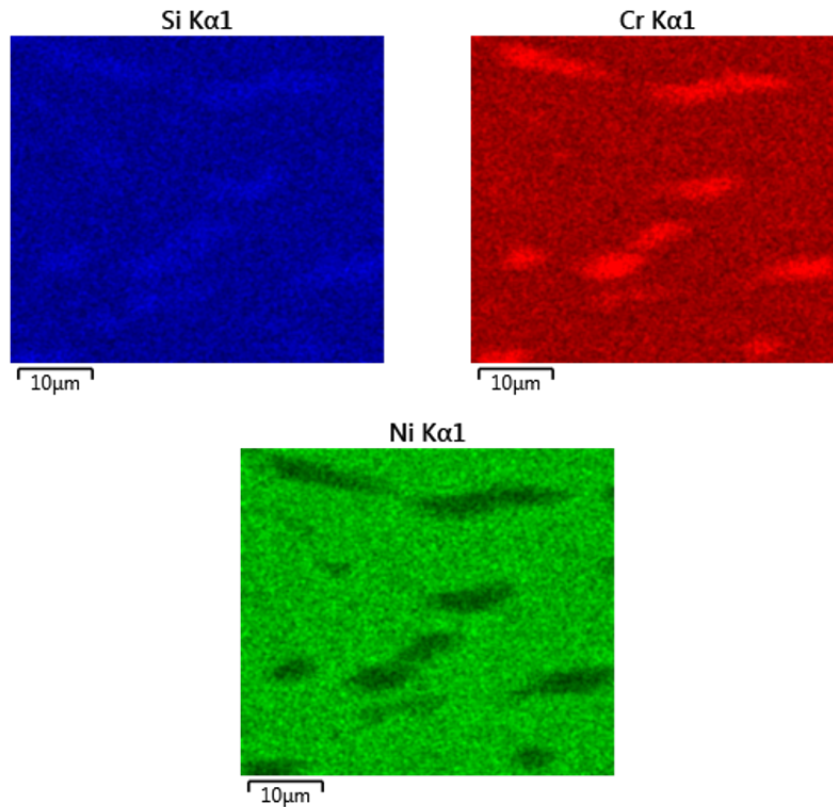
Figure 4.25: SEM EDS maps showing the distribution of Si, Cr, and Ni in the as-cast M_2Si-1.2 specimen. The maps show that the dark grains are rich in Si and Cr, and poor in Ni relative to the matrix phase.

Figure 4.26 shows a selected range of the X-ray diffractogram of the as-cast sample, matched with the Fe_5Si_3 and Ni_2Si crystal structures, tuned with the same cell parameters as those found for M_2Si-1.1. The range was selected to display the most prominent peaks. The full diffractogram can be viewed in chapter 8.

Figure 4.26: Powder XRD of the as cast state of M_2Si-1.2, matched with the structures and lattice parameters found in M_2Si-1.1. The match shows good agreement with the experimental data, showing that the phases in the sample take the Fe_5Si_3 and Ni_2Si crystal structures.

4.3.2 M$_2$Si-1.2b

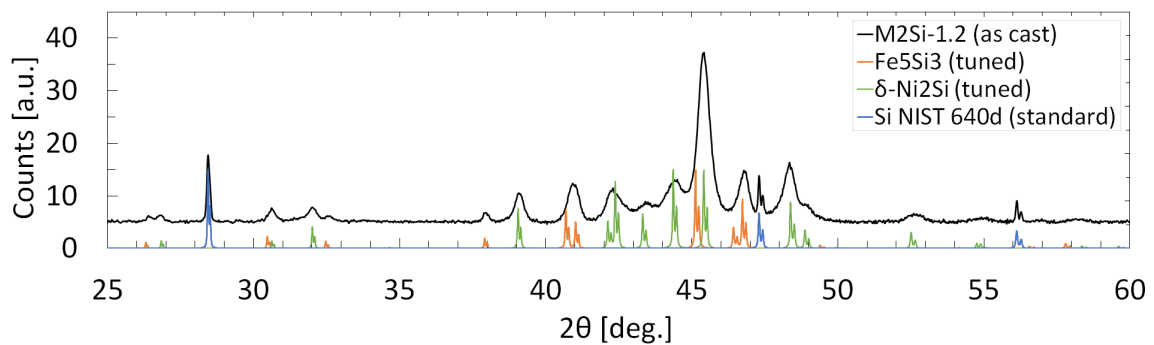To confirm that the results obtained from M$_2$Si-1.1 were reproducible, the M$_2$Si-1.2 specimen was examined by XRD also after annealing. A selected range of the diffractogram, visible in Figure 4.27, showed the same main peaks as the ones found in the as cast sample. The full diffractogram can be viewed in chapter 8. A small peak belonging to the Ni$_2$Si structure could be observed at just under $2\theta = 35°$ which was not distinguishable in the diffractogram of the as cast sample.
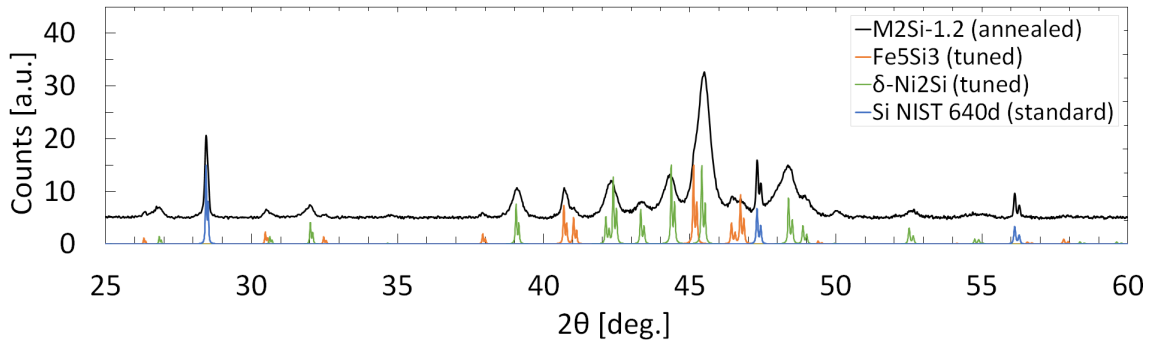

Figure 4.27: Powder XRD of the annealed M$_2$Si-1.2 specimen showing a good match with the Fe$_5$Si$_3$ and Ni$_2$Si structures tuned with the lattice parameters from the M$_2$Si-1.1 diffractogram.

The positions of the peaks in the recorded diffractograms from the as-cast and annealed samples are very similar, as can be seen in Figure 4.28. The relative intensities of the different peaks were slightly different, even though the two diffractograms were obtained under identical conditions. In general the peaks corresponding to the Fe$_5$Si$_3$ structure (phase 1 in M$_2$Si-1.1) were slightly less intense relative to the Ni$_2$Si peaks in the annealed sample as compared to the relative intensities from the as cast sample.
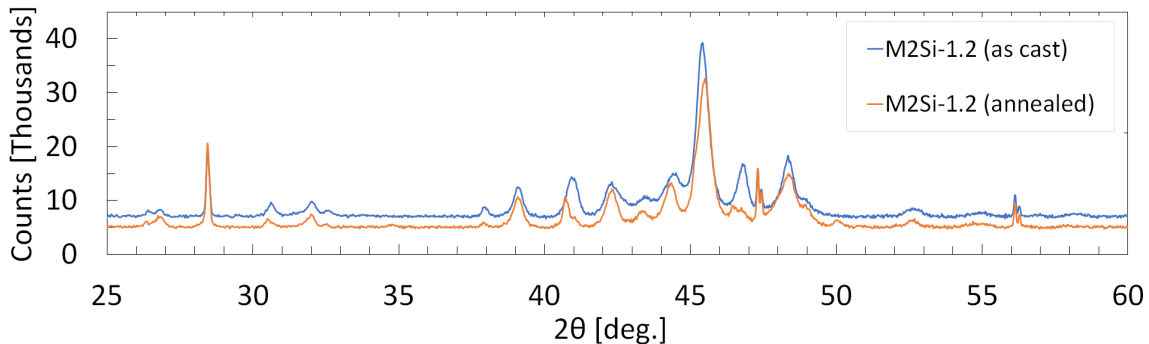
Figure 4.28: Direct comparison of peak intensities in the diffractograms, showing a lower intensity in peaks corresponding to the Fe$_5$Si$_3$ structure, and a slightly higher intensity in Ni$_2$Si peaks in the annealed sample relative to the as cast sample.

Bulk alloy resistivity and Seebeck coefficient

Since no single-phase samples could be produced, electrical resistivity and Seebeck coefficients were measured on the annealed bulk samples from 0-700 °C. The resistivity measurements showed an electrical resistivity on the order of $0.55\,\mu\Omega$ which varied very little with temperature. The resistivity curve, measured both upon heating and cooling can be seen in Figure 4.29.
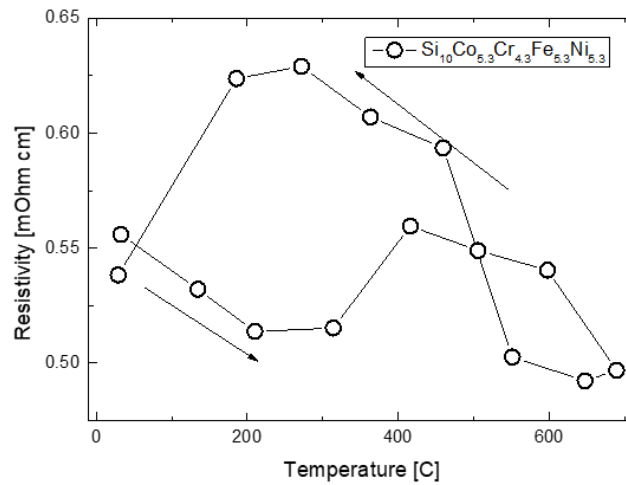
Figure 4.29: Resistivity curve of the annealed bulk M_2Si-1.2 alloy., measured over a temperature range from 0-700 °C The measured resistivity varied very little over the measured temperature range, which is also the reason why the difference between the heating and cooling curve looks much larger than it really is.

The measured Seebeck coefficient was negative, indicating electrons as the majority charge carriers, and very small. The highest absolute value measured for the sample was around $-2.5\,\mu V\,K^{-1}$, measured at 650 °C during cooling. The graph for the measured Seebeck coefficient can be seen in Figure 4.30.
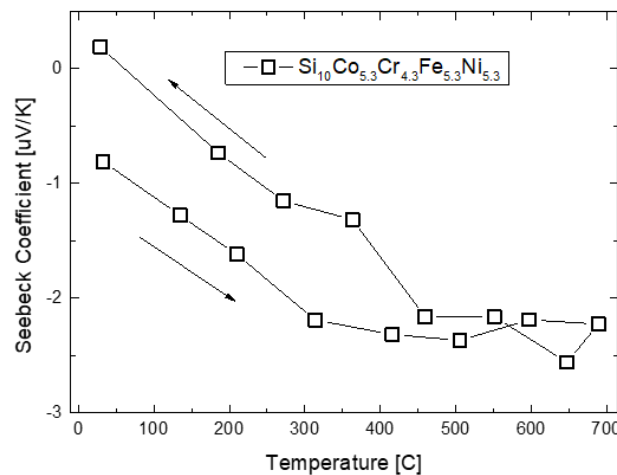
Figure 4.30: Measured values of the Seebeck coefficient of the annealed M_2Si-1.2 bulk sample. Results show a very small, negative Seebeck coefficient with a maximum absolute value of about $-2.5\,\mu V\,K^{-1}$ measured at 650 °C during cooling.

Chapter 5

Discussion

5.1   Cu as a HEA Element

The segregation of a Cu-rich phase from the initial M_2Si-1.0 alloy is consistent with what has been observed previously in the metallic CoCrFeNi HEA. The addition of Cu was reported to lead to the formation of a Cu-rich interdendrite phase without affecting the CoCrFeNi SS much [38]. The observation that annealing did not improve the Cu solubility in the phases further strengthened the conclusion that Cu was not a suitable solute element for this HEA system.

5.2   Phase Identification

The complex microstructure and small grain size in the annealed sample was a result of the single matrix phase of the as-cast specimen segregating, causing growth of two, equally structured phases creating what is referred to as a Widmanstätten pattern [37]. This feature made observations of single phases a challenging task, especially with regards to the acquisition of SAED patterns of phase 3. Since single-phase samples could not be produced, overlapping diffraction signals in both XRD and SAED could somewhat reduce the confidence in the identification of phase 3. However, the high resolution STEM HAADF image shown in Figure 4.17 does contribute significantly towards confirming the structure match that was made.

The XRD data from the annealed M_2Si-1.1 sample also substantiates the conclusion that both matrix phases took the same crystal structure. If there had been a third major phase with a different crystal structure in the sample, there would in all probability have been peaks in the diffractogram that could not be accounted for by the two previously identified structures. The overlap of peaks from phases 2 and 3 in the XRD data also means that the tuning of the lattice constants must necessarily be somewhere in between the actual values for the two separate phases. This observation explains much of the discrepancy in the matches between experiment and simulation for the SAED data obtained for these two phases.

The extra width in the Ni_2Si peaks in the M_2Si-1.1 X-ray diffractogram can be explained by the *almost* complete overlap of the peaks from phases 2 and 3. Two peaks from identical crystal structures with only slight differences in their lattice parameters will look exactly like one wide peak at the resolution that was achievable in the XRD measurements, in accordance with the results in this project. Some of the peak width can probably also be attributed to strain in the crystal structures due to the compositional disorder.

The high-resolution HAADF STEM images in Figures 4.13 and 4.17, together with the Si:M ratios measured by EDS from the three identified phases indicate that the structures were only disordered on their metal sites, while the silicon lattice appeared to be completely ordered. This casts some doubt into whether the phases can indeed be classified as high-entropy alloys, or if they fall under some other category completely. The choice has been made in this thesis to use the compositional HEA definition, which states that phases 2 and 3 fall within the HEA category, while phase 1 falls just outside. However, as mentioned in section 1.2.2, convention allows for classifying this phase too as a HEA [25].

5.2.1 Atomic size effects

The Fe_5Si_3 crystal structure of phase 1 has two non-equivalent metal sites, with the Fe1 6g site having longer Fe-Fe bonds than the Fe2 4d sites ($\sim$2.84 Å and $\sim$2.37 Å, respectively), as shown in 5.1. This non-equivalency could possibly lead to some preferential ordering of the solute phase 1 metal atoms in the structure, or shifting of the atomic positions, or probably both. The non-equivalent sites and corresponding inter-atomic distances could be easily observed and measured in Vesta using the same .cif-files used previously in the project.
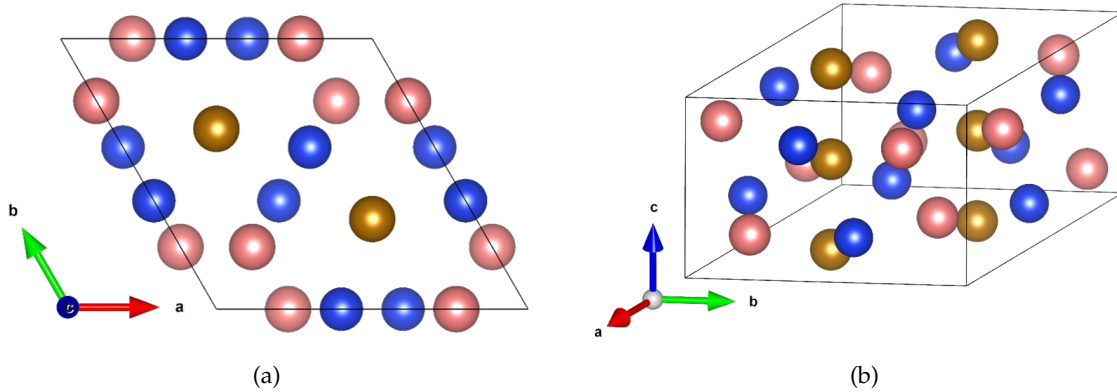

(a)   (b)

Figure 5.1: Unit cell of Fe_5Si_3 with the Fe1 6g positions shown in pink and the Fe2 4d sites shown in gold.

From the atomic radii of the solute metal atoms in all three main phases that can be seen in table 5.1, it may be reasonable to assume that the larger chromium atoms might prefer the Fe1 6g site in the Fe_5Si_3 structure of phase 1 over the Fe2 4d sites with the shorter M-M bond distance. The picture might not be this simple though, as the Fe1 sites have a shorter Fe-Si distance in one direction than what is found in the Fe2 site ($\sim$2.36 Å and $\sim$2.37 Å, respectively). The 6g site also has a greater variation in inter-atomic distances, which could possibly allow for larger shifts in the atom position in this site. Atomically resolved EDS in the [001] orientation of the crystal can help resolve this question. However, this was not achieved within the time frame of this project.

Element	atomic radius [Å]
Cr	1.66
Fe	1.56
Co	1.52
Ni	1.49

Table 5.1: Atomic radii of the 3d transition metals in all three main phases of M_2Si-1.1. Values taken from the CrystalMaker® atomic radii tables [39]

The fact that the main compositional difference between phase 2 and 3 is found in their relative chromium contents can possibly be explained by the differences in atomic radii of the solute atoms on the metal sites of the structures.

As Cr is the element with the largest atomic radius of the four metals found in this alloy system, it is reasonable to think that this would not mix as easily into the Ni_2Si structure of phase 2 as the other metals.

This argument falls somewhat flat on the fact that phase 3 also adopts the same crystal structure, but the probable strain resulting from such a large difference in atom sized on the metal site may be the reason why phase 3 shows so many defects relative to phase 2.

5.2.2   Microstructure and orientation relationships

The hexagonal crystal structure of phase 1 was visible in the microstructure, as approximate 120° angles could be observed along the edges of the phase 1 grains in several places. This can be seen in both Figures 4.3 and 4.24.
.

The orientations of the phase 2 and 3 grains in the annealed M_2Si-1.1 sample show clear preferences for specific orientations of grains and grain boundaries. The systematic orientations of the grains of the two phases were similar to a Widmanstätten type microstructure, not unlike what was observed in the $Al_{0.5}CoCrCuFeNi$ HEA in [31]. This selective orientation happens due to the common crystal structures of the phases having specific planes where the interface energies will be lower than others. Whether this is because of the lattice mismatches being less pronounced in some orientations than others or because of some other reason is unclear.

It is clear from the many orientations of the phase 2 and 3 grains visible from the overview image in Figure 4.3 that the orientation relationship found between phase 2 and 3 in figures 4.18 and 4.19 is not the only one there is. The orientation relationship that was identified may still be worth noting, as the phases did not align completely along the interface, but instead appeared to be mirrored along one of the axes. The ZA used for the diffraction match was the [1-11], indicating a mirroring along the b axis, but both the [-111] and [11-1] ZA patterns would also have been matches, as they are identical in appearance. The [1-11] ZA was chosen as the most likely one given the common [10-1] crystallographic direction found when using this particular ZA for the match.

The determination of the orientation of the planar defects in phase 3 was a somewhat challenging task. Finding an area and orientation where the defects could be observed edge-on took a lot of searching and tilting on very small grains, but when the correct orientation could be found, identifying the correct ZA could be done. Although the FFT match was only approximate, this could be explained by the inaccurate tuning of the cell parameters given from the overlap of the phase 2 and 3 peaks in the XRD data.

When looking at the simulated structure model in Figure 4.23, it seems probable that the defect visible in phase 3 is a fault in the stacking order of the dense layers in the [012] direction, even if it is difficult to say for certain if there would be any preference for the fault to appear in any specific layers over any others.

It does seem logical that the faults would appear in phase 3 over phase 2, as the strain in the crystal structure is probably larger in phase 3 relative to phase 2 due to the higher chromium content. The Ni_2Si structure has been shown to exhibit a highly anisotropic compressibility due to its higher valence-electron density along the c-axis [40]. Due to this anisotropy and the prescence of the layered structure in the [012] direction, stacking fault defects would seem like a good way to release some of the structural strain.

The energies of stacking faults relative to the bulk material is lowered by alloying and distortions in the crystal lattice due to differently sized solute atoms [24, p.83]. It is therefore no surprise that phase 3 would form multiple stacking faults all though its matrix. One explanation for the fact that the faults only seemed to appear in phase 3 could be that atomic size differences created a greater amount of distortions in the crystal lattice in this phase relative to the other two.

Low stacking fault energy can also increase the probability of twinning [24, p. 86], as indicated by the periodic changes in stacking fault orientations observed in several of the phase 3 grains. No SAED patterns were obtained which could prove this, but the observations that could be made in the acquired images of this phase makes it likely.

5.3 M_2Si-1.2

As the M_2Si-1.2 specimen appeared to have some small changes in nominal composition relative to M_2Si-1.1, there cannot be a direct comparison of the two. However, since the phases in M_2Si-1.1 seemed to have some wiggle room with regards to composition, it is a safe assumption to say that the differences between the specimens would not be too significant.

5.3.1 As cast

The most pressing question regarding this sample was what would be the difference between the structure and phase(s) of the matrix before and after annealing, and these questions were answered to some extent by the SEM and XRD results. As the experimental XRD could be comfortably matched with the same structures as those found in the M_2Si-1.1 specimen, it was clear that the high-temperature structures of the phases were similar to the structures at 900 °C. However, the apparent lack of a Widmanstätten structure visible in the SEM image in Figure 4.24 indicates that the segregation of the matrix into two separate, isostructural phases only happened during annealing.

The width in the Ni_2Si peaks of the as-cast alloy can therefore not be attributed to the overlap of peaks from similar phases, but could very well be explained by the assumed strain in the structure due to size mismatch of the solute metal atoms.

5.3.2 After annealing

As expected, the structures found by XRD in the specimen after annealing were the same as those found in the M_2Si-1.1 specimen and in the as-cast M_2Si-1.2 specimen. There were some differences in the relative intensities of the Fe_5Si_3 and Ni_2Si XRD peaks between the obtained diffractograms for the as-cast and annealed samples, but this does not necessarily say anything useful about the temperature-dependent evolution of the phases. These samples were made from different areas of the specimen, so there is no guarantee that the distribution of the different phases would be identical, and therefore, the two diffractograms cannot be directly compared in this way.

The measured electrical resistivity of around $550\,\mu\Omega\,cm$ was slightly higher, but on the same order of magnitude as for conventional HEAs, and a couple of orders of magnitude higher than for conventional alloys. The complex microstructure with relatively small grain sizes could account for the slightly higher than expected resistivity. The low temperature dependence is also typical for HEAs, however the resistivity of these tend to increase with increasing temperature, as is also the case for conventional alloys [9]. This was not the case for the alloy system investigated in this thesis, but the reason for this deviation is unknown.

A very low Seebeck coefficient with an equally low temperature dependence was also measured for the bulk material, revealing together with the measured resistivity values that these materials

are probably metallic and not suitable for thermoelectric uses. This result is unsurprising as the binary silicides Fe_5Si_3 and Ni_2Si are also metallic and not shown to exhibit any notable thermoelectric properties.

No single-phase samples could be produced within the time frame of this project, meaning that the measured resistivity and Seebeck coefficient are properties of the multi-phase bulk, and not the single phases. Consequently, these exact properties are still unknown for the single phases. There are still many more questions to be answered regarding the microstructure, stability and properties of this alloy, and I believe this project has just begun scratching the surface.

Chapter 6

Further Work

There are still many questions to be answered regarding the structure and properties of the phases in these samples, and their structural and functional interactions. This chapter will attempt to briefly address some of these questions, with suggestions for some ways to answer them.

Due to the common structure types of phase 2 and 3, overlap in the XRD signals from the phases means that we still do not know the exact lattice parameters for these phases. Attempting to create single-phase samples would be one way to gain this information. If one or both of these phases are not stable as single phase samples, approximate values could be found through structural relaxation in first-principles calculations, even though these would necessarily be the values seen at $0\,\mathrm{K}$.

There is much work that could be done by first-principles calculations on the different phases. The question of preferential placement of the different solute atoms in the non-equivalent Fe sites in Fe_5Si_3 could perhaps be determined by comparing relative energies of crystals with and without preferential ordering. DFT could also help shed some light on the stability of phase 3. Due to the segregation and huge amount of defects occurring in the matrix phase of the system after annealing, there is some doubt whether phase 3 is an equilibrium phase or if it is only stabilized by the surrounding matrix.

Although it was determined that the bulk material was a poor TE material due to its low Seebeck coefficient, the fact that the measurements were performed on a multi-phase sample means that we still do not know the contributions for each of the phases separately. For this purpose, the production of single-phase samples would be very helpful. However, as the measured Seebeck coefficient of the bulk sample was almost impressively small, the probability of finding promising TE properties in any single-phase sample is minimal.

As a further step in understanding the nature of the defects in phase 3, atomically resolved imaging of the stacking faults in phase 3 could be done as a further step in identifying the specific fault and Burgers vector of the defect.

Further electron diffraction experiments could be done in the phase 2/3 interfaces to determine the other habit planes between the grains in the Widmanstätten microstructure, as it is clear from imaging that there are preferred orientations of interfaces. Electron diffraction on areas containing presumed twin boundaries could also help understand whether the periodic variations in stacking fault orientations is due to twinning. Thermal analysis could also help determine at which temperature the phase transition happens from a single matrix phase to a segregated Widmanstätten microstructure.

Chapter 7

Conclusion

The goal of this project was to produce high entropy silicide alloys using the arc melting method, and to identify any single phases in these samples fitting the HEA definition. Further the goal was to characterize the structure and thermoelectric properties of these phases.

In the course of this project, specimens containing Si, Co, Cr, Fe, Ni, and Cu were produced. Cu was not found to mix well with the other elements and segregated into the interdendritic regions, causing Cu to be abandoned, and new specimens to be created with only the remaining elements. Three silicide phases were identified which can be classified within the high entropy alloy definition. Structural characterization of the phases has determined that all three phases have adopted the structures of known binary silicides.

Phase 1 had a measured composition of $Si_{37}Cr_{22}Fe_{19}Co_{14}Ni_7$, and adopted the hexagonal crystal structure of Fe_5Si_3, with lattice parameters $a = 6.770\,\text{Å}$ and $c = 4.743\,\text{Å}$. The measured compositions of phase 2 and 3 were $Si_{32}Cr_{12}Fe_{17}Co_{19}Ni_{20}$ and $Si_{32}Cr_{18}Fe_{17}Co_{16}Ni_{17}$, respectively, Both of these phases adopted the orthorombic structure of δ-Ni_2Si, but overlapping XRD signals from the two phases meant that exact lattice parameters for each of these phases could not be determined. Measured compositions, as well as atomically resolved HAADF STEM imaging showed that in all three phases, all disorder in the structures appeared to be on the metal sites, with only silicon occupying the silicon sites.

In their as cast state, the specimens appeared to consist of only two main phases, with the Fe_5Si_3 and Ni_2Si structures. After annealing, a segregation of the matrix phase into two (phases 2 and 3) happened, creating a Widmanstätten microstructure. The phase 3 grains also displayed a high density of defects, which were identified as stacking faults in the densely packed atomic layers along the Ni_2Si [012] crystallographic direction.

Measurements of electrical resistivity and Seebeck coefficient were performed on the annealed multi-phase bulk samples, since single-phase samples could not be produced within the time frame of this project. The electrical resistivity was measured around $0.55\,\text{m}\Omega\,\text{cm}$, which is on the same order of magnitude as what has been measured for other HEAs, albeit slightly higher. The maximum measured Seebeck coefficient was $-2.5\,\mu\text{V}\,\text{K}^{-1}$, which is a very small value. This means that the bulk alloy created in this project is not a candidate for thermoelectric uses.

Chapter 8

Appendix

Spot EDS Summary of M$_2$Si$^-_1$ Powder Sample

Si	Cr	Fe	Co	Ni	Cu	Comment
11	26	22	20	1	21	HEA composition, not found elsewhere in the sample. Probable measurement error.
33	27	20	13	6	-	HEA composition
37	29	18	11	5	-	HEA composition
34	24	19	12	11	-	HEA composition
34	25	29	14	7	-	HEA composition
39	26	18	11	5	1	HEA composition
38	22	21	13	5	1	HEA composition
35	25	22	14	2	-	close to HEA composition
30	25	24	17	2	3	close to HEA composition
26	32	24	15	1	2	-
25	70	4	1	-	1	-
51	-	2	4	42	-	-
25	1	3	-	14	54	-
11	-	-	1	12	74	Cu grid
15	-	-	1	11	70	Cu grid
17	-	1	1	13	68	-
16	-	1	1	14	68	-
17	-	1	1	18	62	-
21	71	4	1	1	3	-
23	67	4	-	4	-	-

Table 8.1: Color coding of the different compositions is an attempt at grouping similar compositions possibly belonging to the same phases. The pink row is a probable measurement error. Blue rows are non-HEA compositions. Green rows are HEA compositions. Measured compositions are probably highly innaccurate due to uncertainties in sample thicknesses and deconvolution of oxygen signal in EDS spectra.

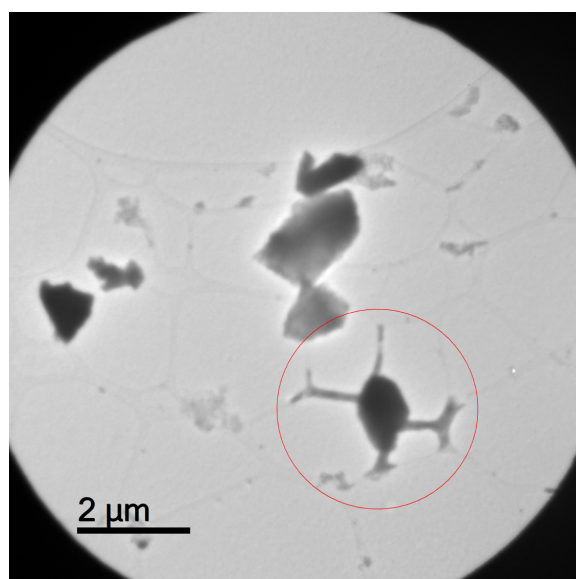# Beam damage on particles in TEM powder samples

Figure 8.1: Low mag. TEM image of beam damaged particle from powder sample. After being illuminated with the electron beam, growth of a segregated phase began along the carbon grid supporting the particle.
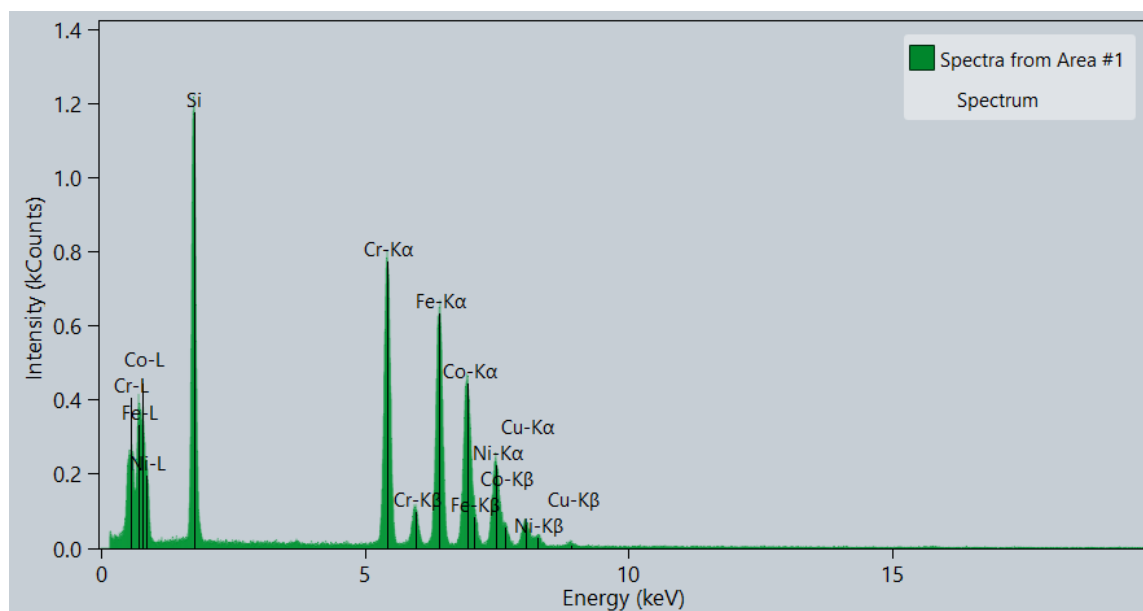
EDS spectra

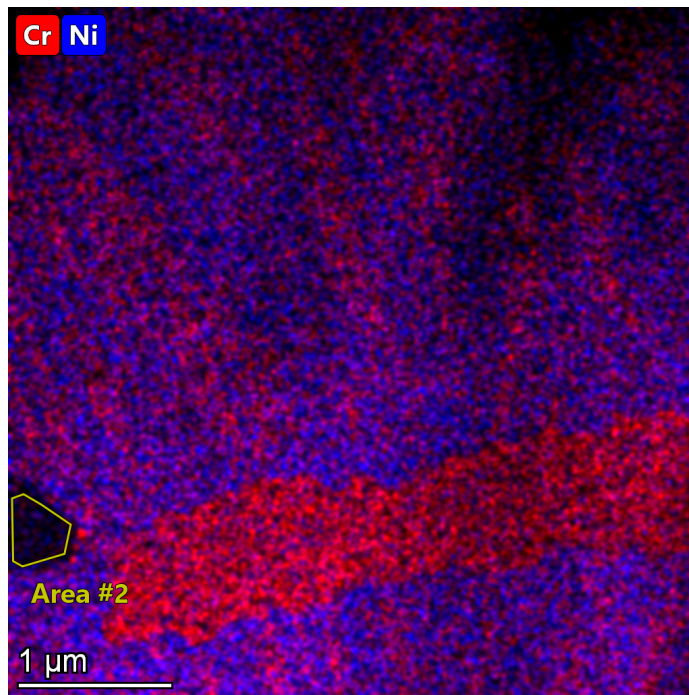Figure 8.2: EDS spectra of area indicated by Figure 4.6 in chapter 4.

Figure 8.3: EDS map of area containing all four phases found in the M_2Si-1.1 sample, with section marked Area #2 showing phase 4.

Element	Family	Atomic Fraction (%)	Atomic Error (%)
Si	K	45.18	4.62
Cr	K	1.44	0.29
Fe	K	18.19	3.05
Co	K	30.44	5.11
Ni	K	4.75	0.82

Figure 8.4: Area #2 (phase 4) EDS composition showing a phase composition too high in silicon and too low in chromium and nickel to be considered a HEA phase.
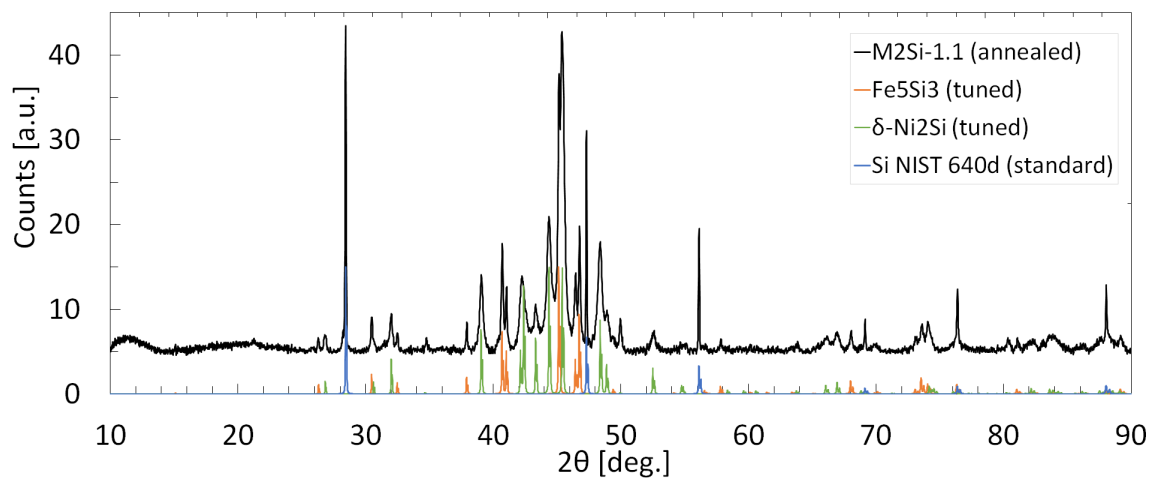
Full X-ray Diffractograms

Figure 8.5: Full recorded diffractogram from the annealed M$_2$Si-1.1 sample. Simulated diffractograms for the Fe$_5$Si$_3$ and Ni$_2$Si structures with tuned lattice constants are also included.

Figure 8.6: Full recorded diffractogram from the as cast M$_2$Si-1.2 sample. Simulated diffractograms for the Fe$_5$Si$_3$ and Ni$_2$Si structures with tuned lattice constants are also included.

Figure 8.7: Full recorded diffractogram from the annealed M_2Si-1.2 sample. Simulated diffractograms for the Fe_5Si_3 and Ni_2Si structures with tuned lattice constants are also included.
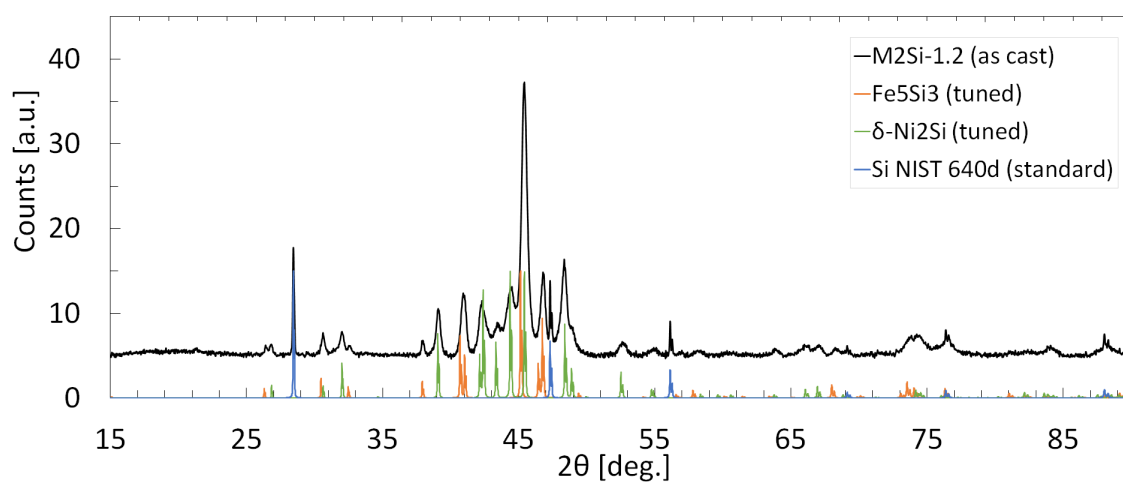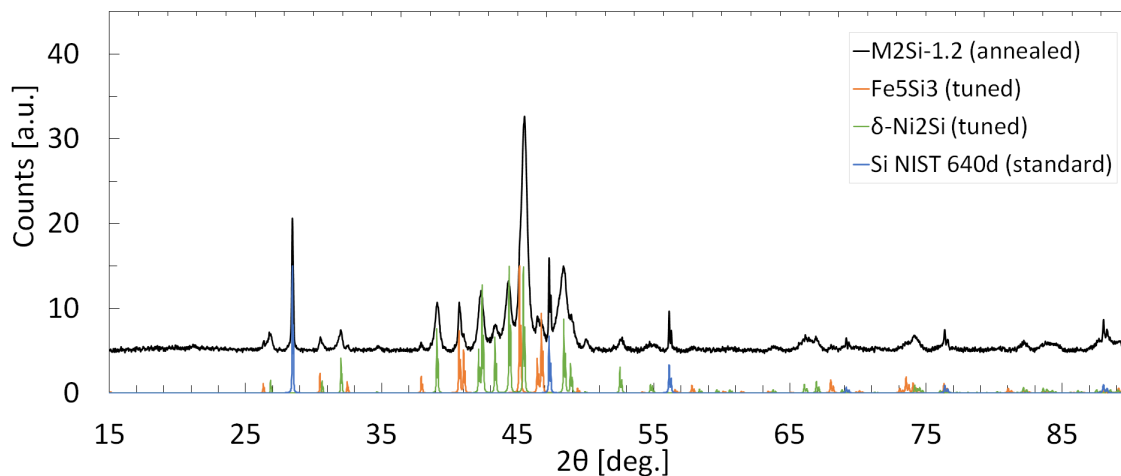
Identifying Phase 3 Stacking Fault Orientation
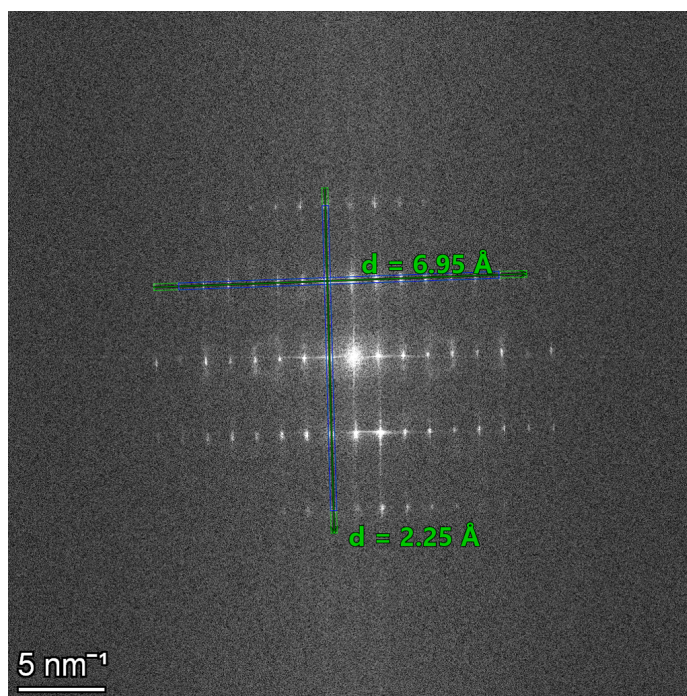
Figure 8.8: Horizontal planar distance measured as 6.95 Å, and vertical planar distance measured as 2.25 Å.

As the a axis of the Ni_2Si structure is the only one large enough to accommodate a planar distance of 6.95 Å, the horizontal lines of reflexes in the DP must belong to the (100) set of planes. By calculating the approximate distances of planes known to be orthogonal to (100), the direction of the vertical lines of reflexes can be found.

We know that for an orthogonal crystal system we have the following relation between planar distances and lattice constants:

$$\frac{1}{d_{hkl}^2} = \left(\frac{h}{a}\right)^2 + \left(\frac{k}{b}\right)^2 + \left(\frac{l}{c}\right)^2 \qquad (8.1)$$

From the measured d value corresponding to the vertical rows of reflexes, we find the experimental value of

$$\frac{1}{d_{exp}^2} = 0.194 \,\mathring{A}^{-2}$$

Using the approximate lattice constants found from fitting of the experimental XRD, we can calculate the $1/d^2$ values for each of the crystallographic planes orthogonal to (100).

$$\frac{1}{d_{011}{}^2} = \left(\frac{1}{5.173 \,\mathring{A}}\right)^2 + \left(\frac{1}{3.759 \,\mathring{A}}\right)^2 = 0.108 \,\mathring{A}^{-2}$$

$$\frac{1}{d_{021}^2} = \left(\frac{2}{5.173 \,\mathring{A}}\right)^2 + \left(\frac{1}{3.759 \,\mathring{A}}\right)^2 = 0.220 \,\mathring{A}^{-2}$$

$$\frac{1}{d_{012}^2} = \left(\frac{1}{5.173 \,\mathring{A}}\right)^2 + \left(\frac{2}{3.759 \,\mathring{A}}\right)^2 = 0.320 \,\mathring{A}^{-2}$$

As the $1/d^2$ value will continue to increase with increasing hkl values, there is no need to calculate any more values. The set of planes with clearly the closest value is the (021) planes, which means that the crystallographic direction viewed in Figure 4.21 is most probably the [01-2] ZA.

Bibliography

1. Riffat, S. B. & Ma, X. Thermoelectrics: a review of present and potential applications. *Applied Thermal Engineering* **23,** 913–935. ISSN: 1359-4311. https://www.sciencedirect.com/science/article/pii/S1359431103000127 (2021) (June 2003).

2. Kittel, C. *Introduction to solid state physics* 8th ed. ISBN: 978-0-471-41526-8 (Wiley, Hoboken, N.J, 2005).

3. Weidenkaff, A. Thermoelectrics: Better half found. *Nature Energy* **2,** 1–2. ISSN: 2058-7546. http://www.nature.com/articles/nenergy201710 (2021) (Feb. 2017).

4. Heremans, J. P. The ugly duckling. *Nature* **508,** 327–328. ISSN: 1476-4687. http://www.nature.com/articles/508327a (2021) (Apr. 2014).

5. Saramat, A., Svensson, G., Palmqvist, A. E. C., Stiewe, C., Mueller, E., Platzek, D., Williams, S. G. K., Rowe, D. M., Bryan, J. D. & Stucky, G. D. Large thermoelectric figure of merit at high temperature in Czochralski-grown clathrate Ba8Ga16Ge30. *Journal of Applied Physics* **99,** 023708. ISSN: 0021-8979. http://aip.scitation.org/doi/full/10.1063/1.2163979 (2021) (Jan. 2006).

6. Brown, S. R., Kauzlarich, S. M., Gascoin, F. & Snyder, G. J. Yb14MnSb11: New High Efficiency Thermoelectric Material for Power Generation. *Chemistry of Materials* **18,** 1873–1877. ISSN: 0897-4756. https://doi.org/10.1021/cm060261t (2021) (Apr. 2006).

7. Yang, S. H., Zhu, T. J., Sun, T., He, J., Zhang, S. N. & Zhao, X. B. Nanostructures in high-performance (GeTe)x(AgSbTe2)100-xthermoelectric materials. *Nanotechnology* **19,** 245707. ISSN: 0957-4484. https://doi.org/10.1088/0957-4484/19/24/245707 (2021) (May 2008).

8. Nozariasbmarz, A., Agarwal, A., Coutant, Z. A., Hall, M. J., Liu, J., Liu, R., Malhotra, A., Norouzzadeh, P., Öztürk, M. C., Ramesh, V. P., Sargolzaeiaval, Y., Suarez, F. & Vashaee, D. Thermoelectric silicides: A review. *Japanese Journal of Applied Physics* **56,** 05DA04. ISSN: 1347-4065. http://iopscience.iop.org/article/10.7567/JJAP.56.05DA04/meta (2021) (Mar. 2017).

9. Tsai, M.-H. Physical Properties of High Entropy Alloys. *Entropy* **15,** 5338–5345. https://www.mdpi.com/1099-4300/15/12/5338 (2021) (Dec. 2013).

10. Burkov, A. T. Silicide Thermoelectrics: Materials for Energy Harvesting. *physica status solidi (a)* **215,** 1800105. ISSN: 1862-6319. http://onlinelibrary.wiley.com/doi/abs/10.1002/pssa.201800105 (2021) (2018).

11. Bennett, G. L. Mission interplanetary: Using radioisotope power to explore the solar system. *Energy Conversion and Management. Space Nuclear Power and Propulsion* **49,** 382–392. ISSN: 0196-8904. https://www.sciencedirect.com/science/article/pii/S0196890407002609 (2021) (Mar. 2008).

12. Dismukes, J. P., Ekstrom, L., Steigmeier, E. F., Kudman, I. & Beers, D. S. Thermal and Electrical Properties of Heavily Doped Ge-Si Alloys up to 1300°K. *Journal of Applied Physics* **35,** 2899–2907. ISSN: 0021-8979. http://aip.scitation.org/doi/abs/10.1063/1.1713126 (2021) (Oct. 1964).

13. Wang, X. W., Lee, H., Lan, Y. C., Zhu, G. H., Joshi, G., Wang, D. Z., Yang, J., Muto, A. J., Tang, M. Y., Klatsky, J., Song, S., Dresselhaus, M. S., Chen, G. & Ren, Z. F. Enhanced thermoelectric figure of merit in nanostructured n-type silicon germanium bulk alloy. *Applied Physics Letters* **93,** 193121. ISSN: 0003-6951. http://aip.scitation.org/doi/full/10.1063/1.3027060 (2021) (Nov. 2008).

14. Joshi, G., Lee, H., Lan, Y., Wang, X., Zhu, G., Wang, D., Gould, R. W., Cuff, D. C., Tang, M. Y., Dresselhaus, M. S., Chen, G. & Ren, Z. Enhanced Thermoelectric Figure-of-Merit in Nanostructured p-type Silicon Germanium Bulk Alloys. *Nano Letters* **8,** 4670–4674. ISSN: 1530-6984. https://doi.org/10.1021/nl8026795 (2021) (Dec. 2008).

15. Satyala, N. & Vashaee, D. Detrimental influence of nanostructuring on the thermoelectric properties of magnesium silicide. *Journal of Applied Physics* **112,** 093716. ISSN: 0021-8979. http://aip.scitation.org/doi/full/10.1063/1.4764872 (2021) (Nov. 2012).

16. LaBotz, R. J., Mason, D. R. & O'Kane, D. F. The Thermoelectric Properties of Mixed Crystals of Mg2Ge x Si1 - x. *Journal of The Electrochemical Society* **110,** 127. ISSN: 1945-7111. http://iopscience.iop.org/article/10.1149/1.2425689/meta (2021) (Feb. 1963).

17. Uher, C. & Miyazaki, Y. in *Materials Aspect of Thermoelectricity* 421–436 (CRC Press, Nov. 2016). ISBN: 978-1-4987-5491-0.

18. Zhou, A. J., Zhu, T. J., Zhao, X. B., Yang, S. H., Dasgupta, T., Stiewe, C., Hassdorf, R. & Mueller, E. Improved Thermoelectric Performance of Higher Manganese Silicides with Ge Additions. *Journal of Electronic Materials* **39,** 2002–2007. ISSN: 1543-186X. https://doi.org/10.1007/s11664-009-1034-6 (2021) (Sept. 2010).

19. Luo, W., Li, H., Fu, F., Hao, W. & Tang, X. Improved Thermoelectric Properties of Al-Doped Higher Manganese Silicide Prepared by a Rapid Solidification Method. *Journal of Electronic Materials* **40,** 1233. ISSN: 1543-186X. https://doi.org/10.1007/s11664-011-1612-2 (2021) (Mar. 2011).

20. Dasgupta, T., Etourneau, J., Chevalier, B., Matar, S. F. & Umarji, A. M. Structural, thermal, and electrical properties of CrSi2. *Journal of Applied Physics* **103,** 113516. ISSN: 0021-8979. http://aip.scitation.org/doi/full/10.1063/1.2917347 (2021) (June 2008).

21. Upadhyay, N. K., Kumaraswamidhas, L. A., Gahtori, B., Bathula, S., Muthiah, S., Shyam, R., Chauhan, N. S., Bhardwaj, R. & Dhar, A. Enhancement in thermoelectric performance of bulk CrSi2 dispersed with nanostructured SiGe nanoinclusions. *Journal of Alloys and Compounds* **765,** 412–417. ISSN: 0925-8388. https://www.sciencedirect.com/science/article/pii/S0925838818322965 (2021) (Oct. 2018).

22. Sakai, A., Ishii, F., Onose, Y., Tomioka, Y., Yotsuhashi, S., Adachi, H., Nagaosa, N. & Tokura, Y. Thermoelectric Power in Transition-Metal Monosilicides. *Journal of the Physical Society of Japan* **76,** 093601. ISSN: 0031-9015. http://journals.jps.jp/doi/10.1143/JPSJ.76.093601 (2021) (Sept. 2007).

23. Miracle, D. B. & Senkov, O. N. A critical review of high entropy alloys and related concepts. *Acta Materialia* **122,** 448–511. ISSN: 1359-6454. https://www.sciencedirect.com/science/article/pii/S1359645416306759 (2021) (Jan. 2017).

24. Gao, M. C., Yeh, J.-W., Liaw, P. K. & Zhang, Y. *High-Entropy Alloys: Fundamentals and Applications* ISBN: 978-3-319-27011-1 (Springer International Publishing AG, Springer International Publishing, Springer, Cham, 2016).

25. Dahlborg, U., Cornide, J., Calvo-Dahlborg, M., Hansen, T. C., Fitch, A., Leong, Z., Chambreland, S. & Goodall, R. Structure of some CoCrFeNi and CoCrFeNiPd multicomponent HEA alloys by diffraction techniques. *Journal of Alloys and Compounds* **681,** 330–341. ISSN: 0925-8388. https://www.sciencedirect.com/science/article/pii/S0925838816312269 (2021) (Oct. 2016).

26. Yeh, J.-W., Chen, S.-K., Lin, S.-J., Gan, J.-Y., Chin, T.-S., Shun, T.-T., Tsau, C.-H. & Chang, S.-Y. Nanostructured High-Entropy Alloys with Multiple Principal Elements: Novel Alloy Design Concepts and Outcomes. *Advanced Engineering Materials* **6,** 299–303. ISSN: 1527-2648. http://onlinelibrary.wiley.com/doi/abs/10.1002/adem.200300567 (2021) (2004).

27. Cantor, B., Chang, I. T. H., Knight, P. & Vincent, A. J. B. Microstructural development in equiatomic multicomponent alloys. *Materials Science and Engineering: A* **375-377,** 213–218. ISSN: 0921-5093. https://www.sciencedirect.com/science/article/pii/S0921509303009936 (2021) (July 2004).

28. Babilas, R., Łoński, W., Boryło, P., Kądziołka-Gaweł, M., Gębara, P. & Radoń, A. The influence of cooling rate, chromium and silicon addition on the structure and properties of Al-CoCrFeNiSi high entropy alloys. *Journal of Magnetism and Magnetic Materials* **502,** 166492. ISSN: 0304-8853. https://www.sciencedirect.com/science/article/pii/S0304885319327957 (2021) (May 2020).

29. Niu, J., Li, W., Liu, P., Zhang, K., Ma, F., Chen, X., Feng, R. & Liaw, P. K. Effects of Silicon Content on the Microstructures and Mechanical Properties of (AlCrTiZrV)-Six-N High-Entropy Alloy Films. *Entropy* **21,** 75. https://www.mdpi.com/1099-4300/21/1/75 (2021) (Jan. 2019).

30. Jensen, J. K., Welk, B. A., Williams, R. E. A., Sosa, J. M., Huber, D. E., Senkov, O. N., Viswanathan, G. B. & Fraser, H. L. Characterization of the microstructure of the compositionally complex alloy Al1Mo0.5Nb1Ta0.5Ti1Zr1. *Scripta Materialia* **121,** 1–4. ISSN: 1359-6462. https://www.sciencedirect.com/science/article/pii/S1359646216301373 (2021) (Aug. 2016).

31. Tsai, C.-W., Chen, Y.-L., Tsai, M.-H., Yeh, J.-W., Shun, T.-T. & Chen, S.-K. Deformation and annealing behaviors of high-entropy alloy Al0.5CoCrCuFeNi. *Journal of Alloys and Compounds* **486,** 427–435. ISSN: 0925-8388. (2021) (Nov. 2009).

32. Ravindra, N. M., Jariwala, B., Bañobre, A. & Maske, A. *Thermoelectrics: Fundamentals, Materials Selection, Properties, and Performance* ISBN: 978-3-319-96341-9. http://link.springer.com/10.1007/978-3-319-96341-9 (2021) (Springer International Publishing, Cham, 2019).

33. Leng, Y. *Materials Characterization: Introduction to Microscopic and Spectroscopic Methods* 2nd ed. ISBN: 978-3-527-67079-6 (Wiley, Hoboken, 2013).

34. Schrade, M., Fjeld, H., Norby, T. & Finstad, T. G. Versatile apparatus for thermoelectric characterization of oxides at high temperatures. *Review of Scientific Instruments* **85,** 103906. ISSN: 0034-6748. http://aip.scitation.org/doi/full/10.1063/1.4897489 (2021) (Oct. 2014).

35. Williams, D. B. & Carter, C. B. in *Transmission Electron Microscopy: A Textbook for Materials Science* (eds Williams, D. B. & Carter, C. B.) 3–22 (Springer US, Boston, MA, 2009). ISBN: 978-0-387-76501-3. https://doi.org/10.1007/978-0-387-76501-3_1 (2021).

36. Shibata, N. Atomic-resolution differential phase contrast electron microscopy. *Journal of the Ceramic Society of Japan* **127,** 708–714 (2019).

37. Purdy, G. R. in *Encyclopedia of Materials: Science and Technology* (eds Buschow, K. H. J., Cahn, R. W., Flemings, M. C., Ilschner, B., Kramer, E. J., Mahajan, S. & Veyssière, P.) 9575–9578 (Elsevier, Oxford, Jan. 2001). ISBN: 978-0-08-043152-9. https://www.sciencedirect.com/science/article/pii/B0080431526017320 (2021).

38. Wang, X. F., Zhang, Y., Qiao, Y. & Chen, G. L. Novel microstructure and properties of multicomponent CoCrCuFeNiTix alloys. *Intermetallics* **15,** 357–362. ISSN: 0966-9795. https://www.sciencedirect.com/science/article/pii/S0966979506002457 (2021) (Mar. 2007).

39. *Elements, Atomic Radii and the Periodic Radii* May 2021. http://www.crystalmaker.com/support/tutorials/atomic-radii/ (2021).

40. Errandonea, D., Santamaria-Perez, D., Vegas, A., Nuss, J., Jansen, M., Rodriguez-Hernandez, P. & Munoz, A. Structural stability of Fe5Si3 and Ni2Si studied by high-pressure x-ray diffraction and ab initio total-energy calculations. *Physical Review B* **77,** 094113. ISSN: 1098-0121, 1550-235X. http://arxiv.org/abs/0803.1722 (2021) (Mar. 2008).